

POLITECNICO DI TORINO



**Politecnico
di Torino**

Master's Degree in Aerospace Engineering
Master's Degree Thesis

Skip Entry Strategy for Vehicle Re-entry

Supervisor:
Prof. Lorenzo Casalino

Candidate:
Dorothy Varrati

TAS-I Advisors:
Ing. Martins Sudars
Dr. Giorgio Fasano

April 2025

Abstract

This dissertation presents the development of a guidance algorithm for the re-entry of a low Lift-to-Drag (L/D) ratio vehicle returning from the Moon, employing a skip entry strategy inspired by the Apollo guidance system. The primary goal of the algorithm is to guide the vehicle from the first atmospheric entry interface to the second, while ensuring that structural stress and thermal loads remain within tolerable limits for the vehicle. To achieve this, a Numerical Predictor-Corrector technique was implemented, utilizing bank angle modulation to control the vehicle trajectory.

The predictor component numerically integrates the complete, unsimplified equations of motion, ensuring a more accurate representation of the vehicle dynamics compared to simplified models, which may introduce approximation errors affecting guidance precision. The corrector component adjusts the bank angle command at each process cycle and is implemented as a PID (Proportional, Integrative, Derivative) controller, with its gain values optimized using a genetic algorithm.

In nominal scenario, the vehicle consistently achieves high-precision targeting. Monte Carlo analyses incorporating various uncertainties, including variations in atmospheric density, aerodynamic coefficients, and initial entry conditions, highlighted that the vehicle very low L/D ratio limits its control authority. This limitation is particularly evident under conditions of low atmospheric density and reduced lift coefficients, resulting in decreased accuracy in reaching the second Entry Interface Point. The reduction in precision is deemed acceptable, as trajectory errors can be effectively corrected during the final phase of re-entry. The methodologies developed in this research offer a robust framework for future lunar return missions, particularly for vehicles with challenging aerodynamic characteristics.

Table of Contents

List of Tables	IV
List of Figures	V
Acronyms	VIII
1 Introduction	1
2 Problem Overview	3
2.1 Lunar re-entry problem	4
2.2 Skip Entry	5
2.3 Constraints	7
2.4 Target	10
2.5 Vehicle characteristics	10
3 Skip entry guidance strategy	12
3.1 Apollo Guidance Algorithm	12
3.2 Current Approaches to Entry Guidance	15
3.2.1 Applications in real-world Missions	21
4 Model and Guidance Strategy	22
4.1 Problem description	22
4.1.1 Vehicle dynamics	22
4.1.2 Environmental model	24
4.1.3 Guidance	25
4.2 Guidance Strategy	26
4.2.1 Longitudinal Guidance	28

4.2.2	Lateral Guidance	31
4.3	Optimization	32
4.3.1	Mathematical model formulation	33
4.3.2	Numerical approach	35
5	Experimental analysis	37
5.1	Mission Scenario	38
5.1.1	Results	41
5.2	Monte Carlo Analysis	51
5.2.1	Mission scenario results	53
5.3	Future Developements	64
6	Conclusion	66
A	Black Box Optimization	68
B	Genetic Algorithm	70
	Bibliography	73

List of Tables

5.1	First EIP	39
5.2	Second EIP	39
5.3	Aerodynamic properties	39
5.4	Chosen PID controller gains	40
5.5	Monte Carlo Parameter dispersions	52
5.6	Monte Carlo statistical summary	64

List of Figures

1.1	Orion Capsule Re-entry [3]	2
2.1	Skip trajectory	3
2.2	Re-entry strategies	5
2.3	Skip Entry	7
2.4	Orion re-entry module [6]	10
2.5	Dragon crew module [7]	10
3.1	Apollo guidance logic flowchart	13
3.2	Apollo Skip Entry phases	14
3.3	PredGuid Flowchart	18
3.4	FNPEG Flowchart	20
4.1	ECEF reference frame	24
4.2	Bank angle	25
4.3	Bank angle modulation	26
4.4	Guidance algorithm flowchart	28
4.5	Guidance block scheme	29
4.6	Corrector scheme	30
4.7	Bank reversal	31
4.8	Heading error	32
4.9	Black Box Optimization scheme	36
5.1	Simulation model scheme	38
5.2	Trajectory profile	41
5.3	Altitude vs Range	42
5.4	Latitude vs Longitude	42

5.5	Velocity vs Time	43
5.6	Altitude vs Velocity	44
5.7	Flight path angle vs Time	45
5.8	Heading angle vs Time	45
5.9	Bank angle vs Time	46
5.10	Dynamic pressure vs Time	47
5.11	G-Load vs Time	47
5.12	Heat flux vs Time	48
5.13	Heat load vs Time	48
5.14	Range error vs Time	49
5.15	Distance from target vs Time	50
5.16	Final position vs Target position	51
5.17	Distribution of final Positions (complete version)	53
5.18	Distribution of final Positions (refined version)	54
5.19	Altitude vs Range	54
5.20	Velocity vs Time	55
5.21	Altitude vs Velocity	55
5.22	Flight-path angle vs Time	56
5.23	Heading vs Time	56
5.24	Density vs Time	57
5.25	Bank angle vs Time	57
5.26	Dynamic pressure vs Time	58
5.27	G-Load vs Time	58
5.28	Heat flux vs Time	59
5.29	Heat load vs Time	59
5.30	Distribution of final positions with density mapping (complete version)	60
5.31	Distribution of final positions with density mapping (refined version)	61
5.32	Range error distribution	62
5.33	Box-plot of range error (including outliers)	63
5.34	Box-plot of range error (outliers removed)	63

Acronyms

EIP

Entry Interface Point

L/D

Lift-to-Drag ratio

NPC

Numerical Predictor-Corrector

LEO

Low Earth Orbit

FPA

Flight Path Angle

PID

Proportional Integrative Derivative

GA

Genetic Algorithm

BBO

Black Box Optimization

Chapter 1

Introduction

Re-entry guidance technologies for lunar return missions have undergone significant advancements, leveraging insights from both historical designs and modern innovations. The Apollo Command Module marked a groundbreaking milestone in lunar re-entry design. Although designed to perform skip entry maneuver - a technique involving an initial descent into the atmosphere followed by a brief exit - it executed only direct descent trajectories, laying the foundation for future developments [1].

In contrast, the Orion Crew Module, developed under NASA Artemis program [2], is specifically optimized for skip entry trajectories. This method, successfully demonstrated during the Artemis I mission, emphasizes its critical role in modern lunar return missions. Skip entry not only mitigates extreme thermal and mechanical loads but also improves trajectory control and extends the achievable range by briefly exiting the atmosphere after an initial descent.

However, low L/D vehicles encounter distinct challenges, particularly in the context of lunar re-entry. The extreme velocities and unique conditions associated with returning from the Moon demand highly precise guidance algorithms to ensure accurate landing while preserving structural integrity under these demanding circumstances.



Figure 1.1: Orion Capsule Re-entry [3]

This thesis focuses on the development of a guidance algorithm tailored for low L/D re-entry vehicles returning from the Moon or the Gateway, a space station located in a Near Rectilinear Halo Orbit around the Moon that serves as a staging point for lunar missions. The primary objectives are to ensure precise guidance toward the designated target and to minimize thermal and mechanical stresses during re-entry, retaining the vehicle structural integrity.

The structure of this thesis is organized to provide a comprehensive understanding of the problem and the solutions developed. Chapter 2 introduces the re-entry problem with a focus on lunar return missions and the skip entry strategy, detailing key constraints and objectives. Chapter 3 reviews both historical and modern guidance algorithms, highlighting the Apollo system and the predictor-corrector approach used in NASA's Artemis missions. Chapter 4 outlines the problem definition and the simulation model developed in this study, with a particular focus on the implementation of the guidance algorithm and the optimization approach adopted. Chapter 5 discusses the results obtained from the specific mission scenario, evaluating the algorithm's effectiveness and robustness through a Monte Carlo analysis. Finally, the chapter provides a summary of the findings and suggests directions for future research.

Chapter 2

Problem Overview

The following chapter will discuss re-entry, with a focus on lunar re-entry, skip entry strategy, and the associated challenges. The spacecraft under investigation features a design reminiscent of the Dragon capsule, characterized by a low lift-to-drag ratio (L/D). This design significantly influences the vehicle aerodynamic performance, particularly during re-entry.

The study focuses on guiding the vehicle from its initial Entry Interface Point (EIP) to a second EIP, as shown in Figure 2.1.

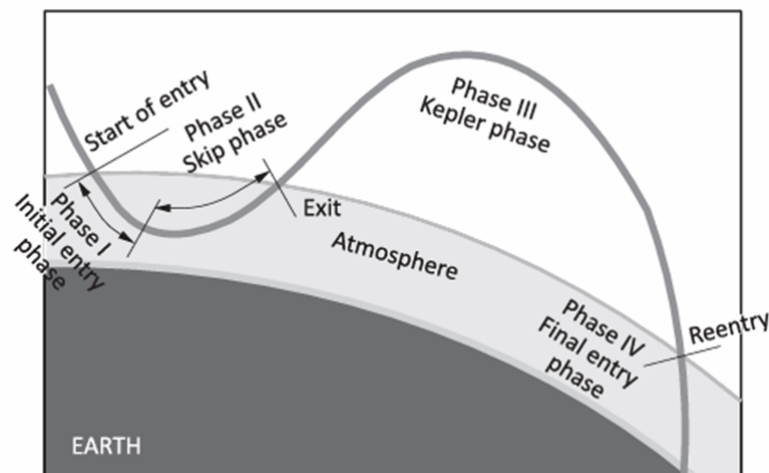


Figure 2.1: Skip trajectory

2.1 Lunar re-entry problem

During the launch phase, a significant amount of kinetic energy must be imparted to the spacecraft to overcome Earth gravitational pull and enable the mission. Conversely, during re-entry, this energy must be dissipated to ensure the vehicle reaches its designated landing site safely.

Two primary strategies exist for energy dissipation during re-entry:

1. **Rocket Braking:** This method employs propulsion to decelerate the vehicle but results in high propellant consumption.
2. **Atmospheric Braking:** This approach leverages aerodynamic drag to dissipate kinetic energy, offering greater efficiency in resource utilization.

Re-entry of a high-velocity spacecraft, such as during a lunar return (~ 11 km/s), presents numerous challenges. The key issues include:

- **Deceleration Loads:** These must remain within tolerable limits for both the vehicle structure and its crew, if present.
- **Aerodynamic Heating:** This arises from convective and radiative heat fluxes on the vehicle surface.
- **Range Control:** Ensuring accurate longitudinal and lateral guidance to achieve the target landing site.
- **Corridor Width:** Maintaining the trajectory within acceptable bounds to prevent either excessive steepness, which could lead to structural failure, or a shallow entry, where the flight path angle is too small, causing the vehicle to skip off the atmosphere instead of descending, potentially resulting in mission failure.

These factors represent the primary constraints of the re-entry problem and will be analyzed in greater detail in subsequent sections.

Re-entry strategies can vary widely based on the mission goals and the vehicle design.

In Figure 2.2 there are three representative trajectories:

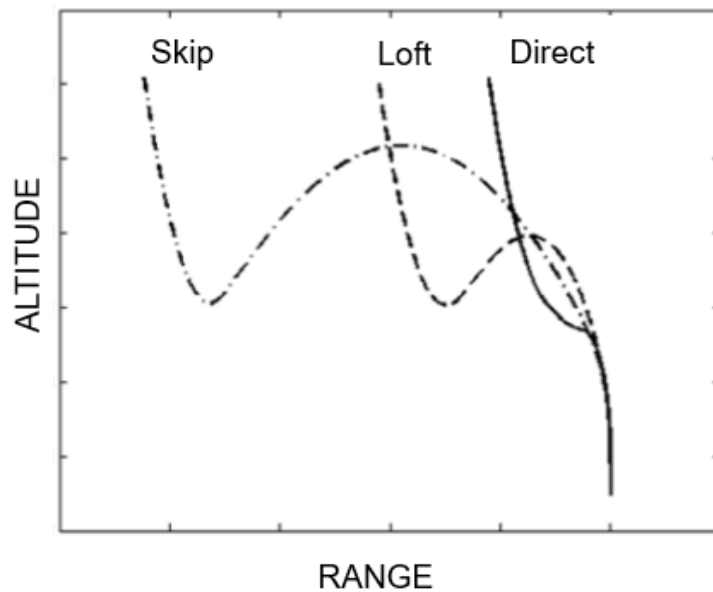


Figure 2.2: Re-entry strategies

- **Direct entry:** the vehicle enters the atmosphere in a straightforward descent.
- **Loft entry:** characterized by a bounce that does not achieve atmospheric exit.
- **Skip entry:** the vehicle exits the atmosphere after the initial entry, then re-enters for the final descent phase.

Each strategy presents distinct benefits, and the best option is selected according to the specific needs of the mission and the vehicle characteristics.

2.2 Skip Entry

The studied vehicle exhibits a low lift-to-drag ratio (L/D), which justifies the use of the skip entry technique. While this characteristic limits maneuverability, it allows the vehicle to efficiently exploit the atmosphere for energy dissipation. While vehicles with higher L/D ratios, such as lifting bodies, can generate greater lift and

achieve more precise control, low-L/D spacecraft can still utilize skip entry with careful selection of parameters such as flight-path angle.

For spacecraft with low L/D ratios, skip entry is an effective re-entry strategy. This technique extends the vehicle range and reduces thermal and aerodynamic loads by modulating its trajectory through the atmosphere. In this context, the range (or downrange) refers to the distance traveled along the arc of the Earth surface, calculated as a portion of the great circle connecting the entry and target points. Similarly, the crossrange describes the lateral deviation from the direct trajectory and is influenced by the vehicle lateral maneuvering capabilities.

A vehicle with an L/D ratio between 0.3 and 0.4, such as Apollo during lunar re-entry, can achieve a maximum range of approximately 3700 km and a crossrange of 110 km with a direct trajectory. However, to further increase range, a skip trajectory can be employed, increasing the altitude before re-entering the atmosphere to allow for a longer glide phase and greater horizontal distance traveled.

In a skip trajectory, the vehicle dissipates energy more gradually, allowing it to achieve greater range and crossrange capabilities.

The skip entry trajectory typically consists of five phases (as illustrated in Figure 2.3):

1. First atmospheric entry.
2. Skip phase: deceleration followed by a brief exit from the atmosphere.
3. Kepler phase: a ballistic trajectory outside the atmosphere.
4. Second atmospheric entry.
5. Final descent phase.

The primary objectives of a skip entry guidance algorithm include:

- Ensuring suitable initial conditions for the final re-entry phase.
- Maintaining gravitational and thermal loads within safe limits.
- Achieving precise targeting.

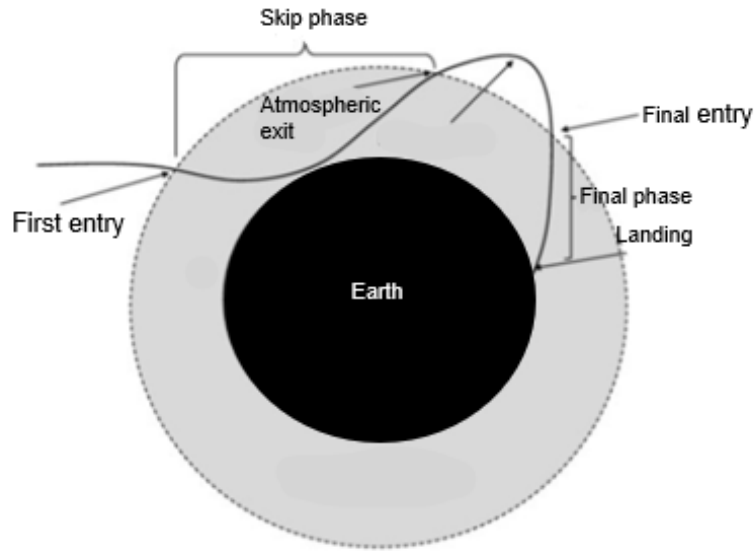


Figure 2.3: Skip Entry

The trajectory planning during the skip phase is particularly critical due to the limited maneuverability of low L/D vehicles. During the Apollo program, a reference trajectory was utilized because the computational constraints of that era did not allow for real-time updates based on actual conditions. Despite these limitations, it was already understood that an adaptive approach to trajectory definition could significantly enhance accuracy, a principle that has become central to modern re-entry guidance systems.

2.3 Constraints

Atmospheric re-entry is governed by fundamental design and operational constraints critical for mission safety and success. The primary constraints include:

1. Dynamic Pressure (q): Dynamic pressure, representing aerodynamic loads on the vehicle, is calculated as:

$$q = \frac{1}{2}\rho V^2 < q_{max} \quad [N/m^2]$$

where,

- ρ : local atmospheric density, a function of altitude,
- V : vehicle velocity relative to the atmosphere,
- q_{max} : maximum admissible dynamic pressure.

Dynamic pressure must remain below a maximum allowable value to prevent structural damage.

2. G-Load (g_{load}): Gravitational loads represent the forces perceived by the crew or internal systems:

$$g_{load} = \frac{\sqrt{L^2 + D^2}}{mg_0} < g_{load\ max}$$

where,

- L : lift force,
- D : aerodynamic drag,
- m : vehicle mass,
- g_0 : gravitational acceleration,
- $g_{load\ max}$: maximum admissible g-load.

This value must stay within tolerable limits for both the structure and crew, if present, to prevent damage to the vehicle and ensure the safety and well-being of the occupants during the re-entry and landing phases.

3. Heat Flux (\tilde{q}): Total heat flux on the vehicle during atmospheric re-entry is the sum of convective and radiative contributions, imposing a critical constraint on the design of the thermal protection system.

- (a) Convective Heat Flux (\tilde{q}_{conv}): Convective heat flux occurs due to the movement of air molecules around the capsule surface at high temperature. Estimated using the Detra-Kemp-Riddell (DKR) empirical formula [4]:

$$\tilde{q}_{conv} = K \frac{1}{\sqrt{R_n}} \left(\frac{\rho}{\rho_0} \right)^{0.5} \left(\frac{v}{v_0} \right)^{3.15} \quad [W/m^2]$$

where,

- K : empirical coefficient,
- R_n : spacecraft nose radius,
- ρ : atmospheric density
- $\rho_0 = 1.225 \text{ kg/m}^3$,
- v : spacecraft velocity,
- v_0 : 10654 m/s.

So this term depends on the vehicle geometry and thermal properties of the heat shield.

- (b) Radiative Heat Flux: The term radiative heat flux takes into account the amount of heat transferred through electromagnetic radiation, which becomes relevant at speeds above 9 km/s, typical of lunar re-entry. Estimated via Tauber-Sutton Relation [5]:

$$\tilde{q}_{rad} = C R_n^a \rho^{1.22} f(V) \quad [W/m^2]$$

where,

- C : empirical coefficient,
- R_n : spacecraft nose radius,
- a : empirical coefficient $f(V, \rho)$,
- ρ : atmospheric density,
- $f(V)$: tabulated velocity function for the Earth atmosphere.

- (c) Total Heat Flux:

$$\tilde{q} = \tilde{q}_{conv} + \tilde{q}_{rad} < \tilde{q}_{max}$$

This value must remain below \tilde{q}_{max} , limit imposed by the available materials, in order to ensure heat shield integrity.

Total heat load is obtained integrating total heat flux over time.

4. Bank Angle Rate ($\frac{d\sigma}{dt}$): The modulation of the bank angle σ is crucial for trajectory control. However, the rate of change $\frac{d\sigma}{dt}$ must be limited for physical reasons.

2.4 Target

The aim of the re-entry trajectory is to achieve a specific landing site. In the context of this thesis it is defined by:

- Target latitude.
- Target longitude.
- Target altitude.

The goal is to ensure precise targeting despite stringent re-entry constraints.

2.5 Vehicle characteristics

The vehicle under investigation is specifically designed for lunar or Gateway return missions.

The vehicle under investigation features a low lift-to-drag ratio (L/D), which is similar to Dragon, shown in Figure 2.5. However, while Dragon is designed primarily for Low-Earth-Orbit (LEO) operations such as servicing the ISS, the present case involves re-entry from the Moon or the Gateway, which imposes far more stringent requirements, particularly concerning thermal protection and trajectory control.



Figure 2.4: Orion re-entry module [6]



Figure 2.5: Dragon crew module [7]

Lunar re-entry vehicles, such as Apollo and Orion, have higher L/D ratios since they present a different angle of attack, this allows greater maneuverability during re-entry. The low L/D ratio of the vehicle presents unique challenges in terms of trajectory planning and control, necessitating a detailed analysis of the re-entry scenario. The vehicle's shape resembles Dragon configuration, which differs from the broader bell shapes of Apollo and Orion, in Figure 2.4.

Chapter 3

Skip entry guidance strategy

The challenge of accurately guiding a spacecraft through atmospheric re-entry has driven the development of various algorithms, each tailored to the specific technological constraints and mission objectives. These strategies have revolutionized space exploration by enabling precise landing capabilities and mission success, despite the challenges of dynamic environments and limited resources.

Skip entry guidance strategies, which exploit aerodynamic lift to extend range and refine landing accuracy, have played a crucial role in re-entry technologies. This chapter provides an overview of two key approaches to skip entry guidance: the Apollo Guidance Algorithm (see e.g. [8]), developed during the Apollo program with its limited computational capabilities, and modern Numerical Predictor-Corrector methodologies, made possible by advancements in on-board computational power.

By analyzing these strategies, the aim is to highlight their evolution, strengths, and limitations, offering a foundation for understanding their application to current and forthcoming re-entry missions.

3.1 Apollo Guidance Algorithm

The Apollo program represented a pioneering effort in re-entry guidance, with its algorithm tailored to the limited computational capabilities of its on-board system. The Apollo baseline guidance system was divided into six distinct phases, as shown in Figure 3.2, designed to manage the vehicle downrange effectively and ensure mission success. These phases collectively balanced computational simplicity with

operational precision, serving as the foundation for subsequent advancements in re-entry technology.

Below, in Figure 3.1, is a simplified depiction of the Apollo algorithm in flowchart form. Initialization occurs only during the first cycle, while navigation, targeting, mode selection, and lateral guidance routines run during every guidance cycle.

The navigation routine collects data from the on-board accelerometers, and the targeting routine updates the vector from the vehicle to the landing site. Next, the phase selector determines which of the six phases of the guidance cycle the vehicle is in by using a parameter called the “selector,” which can take a value from 1 to 6 on each run.

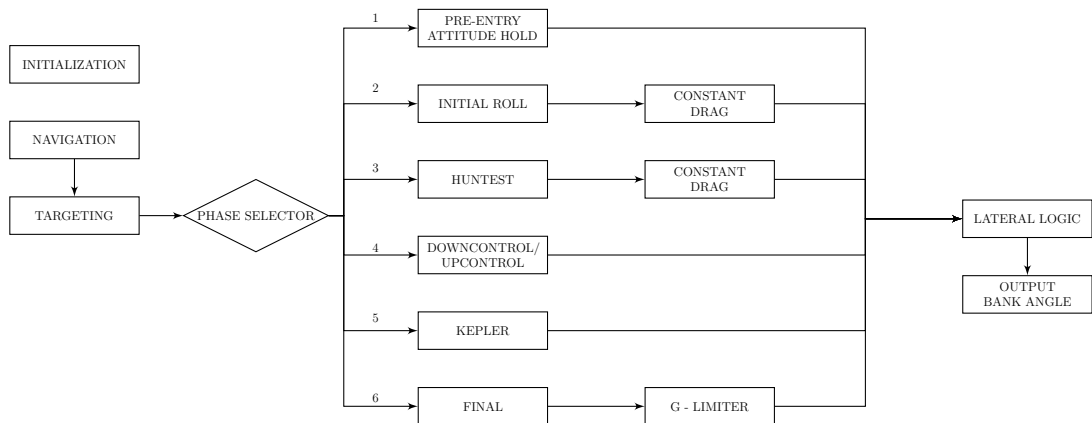


Figure 3.1: Apollo guidance logic flowchart

The six phases along the trajectory are summarized herein.

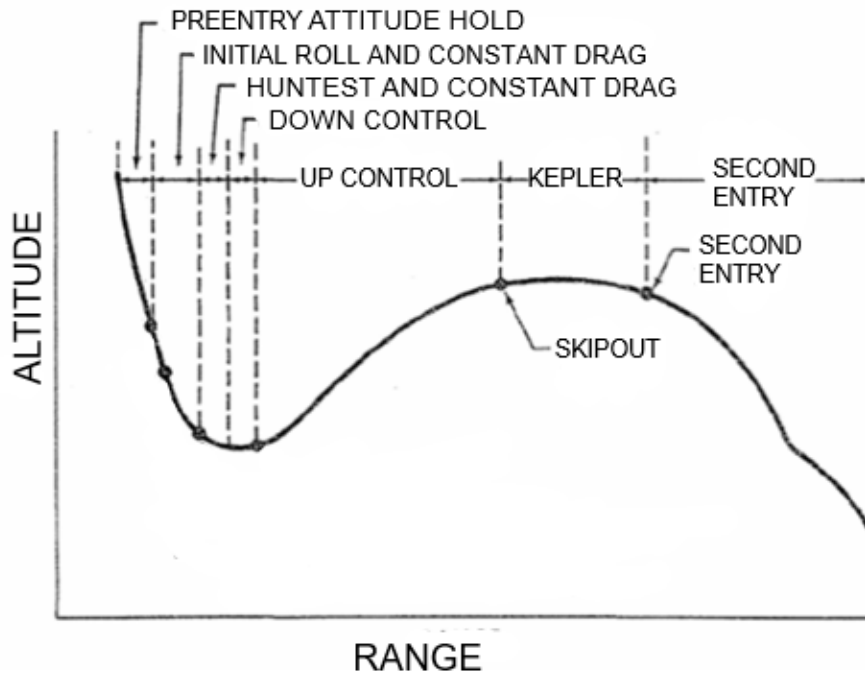


Figure 3.2: Apollo Skip Entry phases

1. **Pre-Entry Attitude Hold:** This phase begins when the guidance system takes control of the vehicle. The command module maintains a fixed attitude along all three axes, preparing for the hypersonic phase of entry. This phase concludes once the sensed atmospheric loading exceeds a threshold, signaling the start of active control.
2. **Initial Roll and Constant Drag:** The vehicle adjusts its lift vector to guide itself towards the center of the re-entry corridor. The primary objectives are ensuring aerodynamic capture and maintaining a safe trajectory through the atmosphere.
3. **Huntest and Constant Drag:** Once aerodynamic capture is confirmed, this phase maintains a constant drag while refining the trajectory to align with the target. The algorithm determines whether a skip maneuver is necessary, based on the calculated downrange error. For shorter ranges, the algorithm transitions directly to the final phase. Roll commands during this phase

are computed analytically, based on drag and range-rate errors relative to a reference trajectory.

4. **Down and Up-Control:** During these phases, the roll commands guide the vehicle along the predicted trajectory. In the up-control phase, a reference-following controller adjusts the vehicle trajectory to match the path defined in the hunttest phase. However, this trajectory is not updated during the phase, limiting the adaptability of the system.
5. **Kepler Phase (ballistic exit):** If the vehicle exits the atmosphere, this phase begins once aerodynamic acceleration drops below a predefined threshold. Due to negligible dynamic pressure, no control authority exists, and the bank angle remains fixed at its last commanded value.
6. **Second Entry and Final Phase:** When aerodynamic acceleration exceeds the threshold again, the vehicle reenters the atmosphere and transitions to the final guidance phase, aiming to land at the target.

Although it was highly innovative for its time, the Apollo guidance algorithm suffered from low landing accuracy. The primary issues were inaccuracies in the predicted exit conditions during the hunttest phase and the lack of trajectory updates in the up-control phase. These limitations were later addressed by replacing the up-control phase with a Numerical Predictor-Corrector (NPC) algorithm, which enhanced precision and adaptability by iteratively refining the trajectory.

3.2 Current Approaches to Entry Guidance

Advancements in computational power since the Apollo program have enabled the development of Numerical Predictor-Corrector (NPC) algorithms for re-entry guidance. These algorithms allow for real-time trajectory determination and optimization, enhancing flexibility and accuracy in response to dynamic conditions.

NPC algorithms operate iteratively, integrating the equations of motion to predict the vehicle final state for a given bank angle profile. Based on the predicted outcome, the algorithm adjusts the bank angle and reruns the simulation until the target is reached. This iterative process is repeated at each guidance cycle, starting

from the current state, ensuring that the vehicle remains on a precise path to its destination.

There are three primary types of predictor-corrector methods [9]:

- **Numerical Predictor-Corrector (NPC):** This approach uses numerical integration of the non-simplified equations of motion. While highly accurate, it requires significant computational resources, making it the most demanding method in terms of onboard processing. The accuracy of NPC makes it particularly well-suited for missions requiring precise targeting.
- **Analytic Predictor-Corrector (APC):** The APC method [10] follows the same iterative process but relies on closed-form solutions of the equations of motion to predict the final state. Although computationally efficient and flexible in accounting for vehicle and atmospheric parameters, the simplifications involved limit its accuracy compared to NPC.
- **Reference-Following Controller:** This method relies on a pre-computed reference trajectory, typically generated before the mission [9]. During flight, the algorithm computes bank angle commands to correct deviations and align the vehicle with the reference. While computationally efficient and straightforward to implement, this method is less adaptable to unforeseen flight conditions due to its reliance on the pre-computed trajectory.

Outlined below are the some examples of NPC algorithms.

A. Numerical Skip Entry Guidance (NSEG):

Developed by NASA/JSC, NSEG combines a high Technology Readiness Levels (TRL) Apollo-based guidance system with a numerical scheme for real-time, long-range skip trajectories [11].

Phases of Operation:

- I. **Numerical Predictor-Corrector:** NSEG calculates the commanded bank angle by iteratively adjusting constant-bank trajectories until the predicted range matches the reference range. It uses the bounded Regula-Falsi method and occasionally reduces the step size to overcome convergence issues. The in-plane trajectory is propagated while maintaining the out-of-plane motion within a crossrange corridor.

- II. **Blending:** A blended bank-angle command is used to transition from the numerical solution to the Apollo final phase solution.
- III. **Apollo Final Phase:** Below an altitude of 120 km, in accordance with the second EIP, the guidance transitions into the third phase, which corresponds to the final phase of Apollo. This phase continues until the velocity decreases to 300m/s.
- IV. **Proportional Steering:** A gain proportional to the heading error generates a bank angle command that guides the vehicle to the target point where parachute deployment occurs.

B. **PredGuid:**

Developed at Draper Laboratory, PredGuid combines the Apollo guidance logic with a modified numerical Predictor-Corrector (NPC) scheme initially designed for aerocapture applications (see e.g. [11] [9] [12]). It replaces the Apollo Down Control, Up Control, and Keplerian phases with a new NPC approach. The modified phases, in comparison to the Apollo algorithm, are outlined below and schematized in Figure 3.3:

- I. **Up Control:** This phase follows the first two phases of the Apollo guidance and replaces both Down Control and Up Control. It ensures the vehicle reaches the desired target range and required velocity by propagating a constant-bank trajectory. If the predicted range-to-go falls outside a defined tolerance, the corrector recalculates the bank angle, and the predictor runs again.
- II. **Ballistic:** This phase replaces the Apollo Ballistic phase, beginning when the vehicle exits the sensible atmosphere. The Predictor-Corrector continues to operate even if the bank command remains unchanged.
- III. **Terminal Guidance:** After final phase entry, a simple proportional guidance system adjusts for any remaining cross range offset in the final phase, using a proportional gain on heading error to generate a bank angle command for guiding the vehicle to the parachute deployment point.

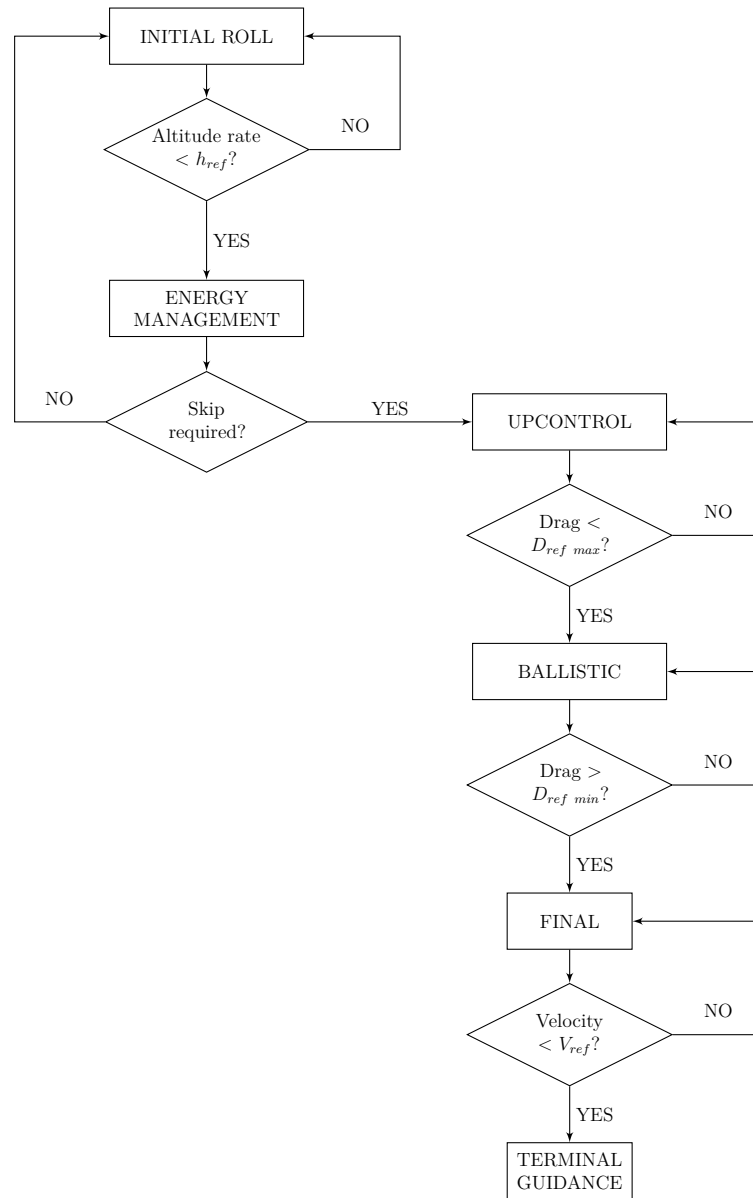


Figure 3.3: PredGuid Flowchart

C. Fully Numerical Predictor-Corrector Entry Guidance (FNPEG):

FNPEG determines the bank angle at each guidance cycle [13]. During the skip phase, the algorithm employs a planning segment where the entire trajectory is simulated, followed by a corrector that iterates to select the bank angle for the next cycle. During the final phase, a similar planning segment is used. In Figure 3.4 a phase transition logic scheme of FNPEG.

The FNPEG algorithm consists of the following phases:

- I. **Initial Entry:** The bank angle is typically held at 0° as it would be ineffective at this stage.
- II. **Down-Control:** As the atmospheric density increases to a sensible level, the bank angle is calculated as a linear function of the range-to-go up to a specified threshold of the skip trajectory segment.
- III. **Up-Control:** When the flight path angle (FPA) becomes positive, the bank angle is again determined in the same manner as in the down-control phase.
- IV. **Kepler:** When bank angle control becomes ineffective, a constant zero bank angle is commanded, marking the transition to a ballistic phase.
- V. **Final phase:** If the range-to-go exceeds 2000 km at any stage, the algorithm transitions to the final phase, where a constant bank angle is commanded. The bank angle is then parameterized as a linear function of energy.

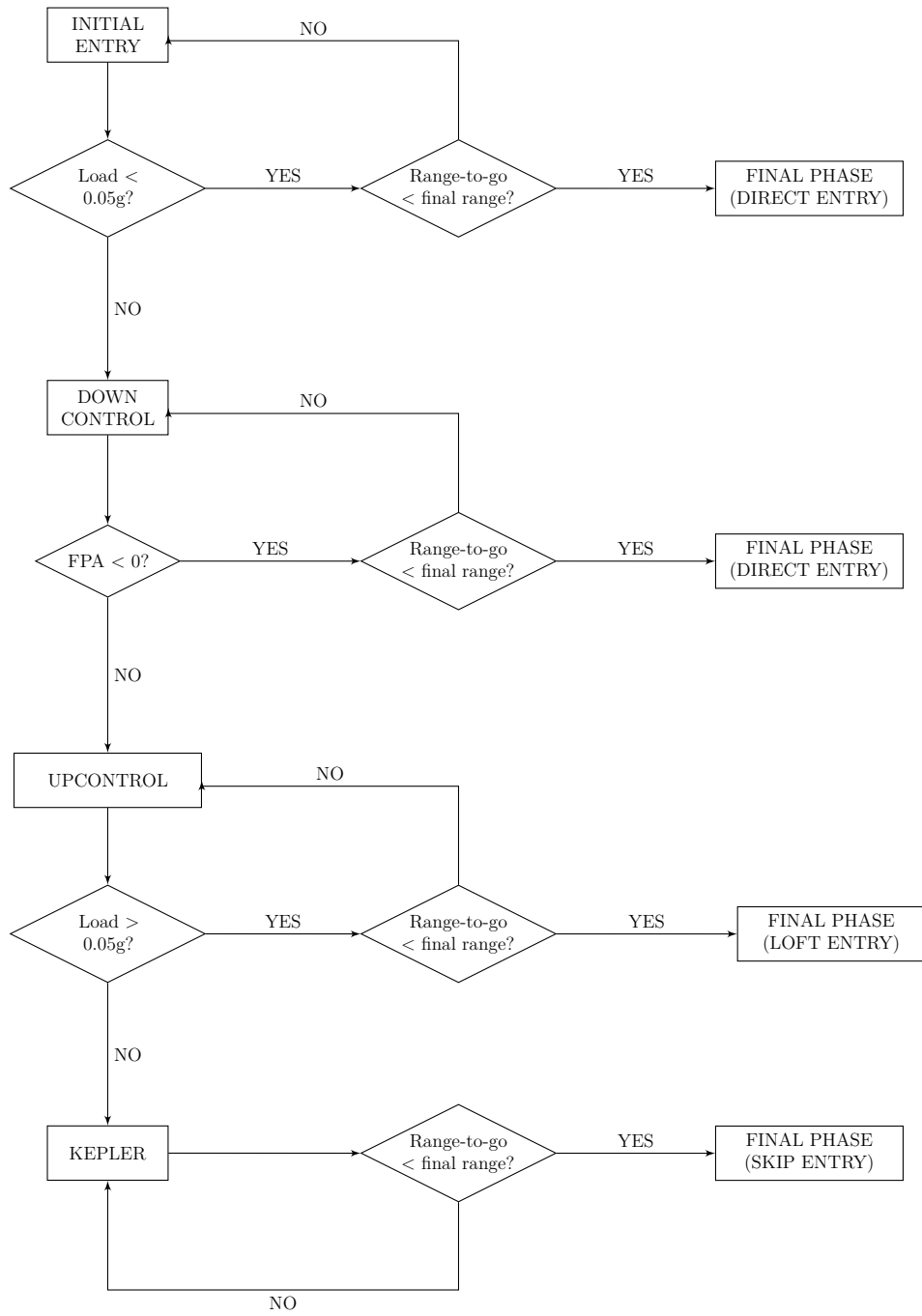


Figure 3.4: FNPEG Flowchart

3.2.1 Applications in real-world Missions

The Orion spacecraft, developed for NASA Artemis program, employs a Numerical Predictor-Corrector approach optimized for lunar return missions. The guidance system determines an optimal bank angle profile in real time, ensuring the vehicle trajectory meets mission objectives while maintaining structural and thermal integrity. For example, during critical re-entry phases, the Orion system dynamically adjusts to account for atmospheric variations, providing unparalleled precision and safety.

NPC algorithms represent a significant improvement over the Apollo-era guidance system, addressing its key limitations. By updating the trajectory dynamically and accounting for nonlinearity in the equations of motion, NPC provides superior precision and adaptability, particularly for challenging scenarios such as skip entry.

In summary, the evolution from Apollo's heuristic guidance system to the Numerical Predictor-Corrector approaches highlights the progress in re-entry guidance strategies. While the Apollo algorithm laid the groundwork, modern computational capabilities have enabled more accurate and versatile guidance methods. These advancements are essential for lunar return missions with low lift-to-drag vehicles and pave the way for future interplanetary missions, such as those to Mars, where precision and adaptability will be crucial for success.

Chapter 4

Model and Guidance Strategy

This chapter focuses on the re-entry guidance of a spacecraft returning from the Moon, emphasizing the challenges of atmospheric re-entry and the strategies employed to ensure precise targeting of the desired second EIP position. The objective is to guide the vehicle from the first Entry Interface Point (EIP) at 120 km altitude, through a skip maneuver, and back to the second EIP at the same altitude. The following chapter details the dynamics of the re-entry problem and the guidance strategy employed to resolve it.

4.1 Problem description

4.1.1 Vehicle dynamics

The vehicle's re-entry dynamics over a rotating spherical Earth are described by the following dimensionless three-dimensional equations of motion (Equation 4.1), expressed in a spherical Earth-Centered Earth-Fixed (ECEF) reference frame [14]. The state vector in the ECEF frame is defined as:

$$\mathbf{x} = [r, \phi, \theta, V, \gamma, \psi]^T$$

where,

- $r(t)$: radial distance from the Earth center,

- $\phi(t)$: latitude,
- $\theta(t)$: longitude,
- $V(t)$: circular velocity,
- $\gamma(t)$: flight path angle,
- $\psi(t)$: heading angle.

$$\left\{ \begin{array}{l} \dot{r} = V \sin \gamma \\ \dot{\theta} = \frac{V \cos \gamma \sin \psi}{r \cos \phi} \\ \dot{\phi} = \frac{V \cos \gamma \cos \psi}{r} \\ \dot{V} = -\frac{D}{m} - \frac{\sin \gamma}{r^2} + \Omega^2 r \cos \phi (\sin \gamma \cos \phi - \cos \gamma \sin \phi \cos \psi) \\ \dot{\gamma} = \frac{1}{V} \left[\frac{L \cos \sigma}{m} + \left(V^2 - \frac{1}{r} \right) \frac{\cos \gamma}{r} + 2\Omega V \cos \phi \sin \psi \right. \\ \quad \left. + \Omega^2 r \cos \phi (\cos \gamma \cos \phi + \sin \gamma \cos \psi \sin \phi) \right] \\ \dot{\psi} = \frac{1}{V} \left[\frac{L \sin \sigma}{m \cos \gamma} + \frac{V^2 r \cos \gamma \sin \psi \tan \phi}{r} - 2\Omega V (\tan \gamma \cos \psi \cos \phi - \sin \phi) \right. \\ \quad \left. + \frac{\Omega^2 r \sin \psi \sin \phi \cos \phi}{\cos \gamma} \right] \end{array} \right. \quad (4.1)$$

with

$$D = \frac{1}{2} \rho V^2 S C_D$$

$$L = \frac{1}{2} \rho V^2 S C_L$$

where,

- r : radial distance from the Earth center,
- D : aerodynamic drag force,
- L : aerodynamic lift force,

- σ : bank angle,
- Ω : Earth angular rotation velocity.

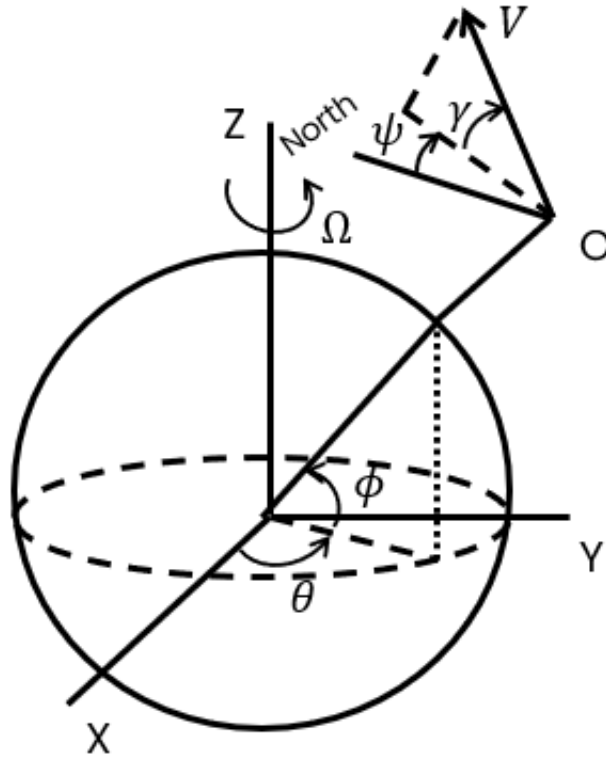


Figure 4.1: ECEF reference frame

The aerodynamic coefficients, lift coefficient (C_L) and drag coefficient (C_D), are considered constant. The integration of the motion equations concludes when the spacecraft reaches the second Entry Interface Point (EIP), returning to an altitude of 120 km.

4.1.2 Environmental model

The environmental model accounts for gravitational acceleration (\mathbf{g}) and atmospheric density (ρ), both of which significantly influence the vehicle's dynamics.

The gravitational acceleration is determined using a simplified model with a spherical Earth assumption.

$$\mathbf{g} = \frac{R_E^2}{r^2} \mathbf{g}_0$$

The atmospheric density is derived from the 1976 U.S. Standard Atmosphere model [15], interpolating values based on the current altitude.

4.1.3 Guidance

The guidance algorithm employs a Numerical Predictor-Corrector methodology. This approach predicts the spacecraft's trajectory and applies corrections to ensure it reaches the desired target.

The primary control parameter used to manage the vehicle's trajectory is the bank angle. The bank angle is defined as the angle between the vehicle's lift vector and the local vertical direction (Figure 4.2).

By adjusting this angle, the spacecraft can control the direction and magnitude

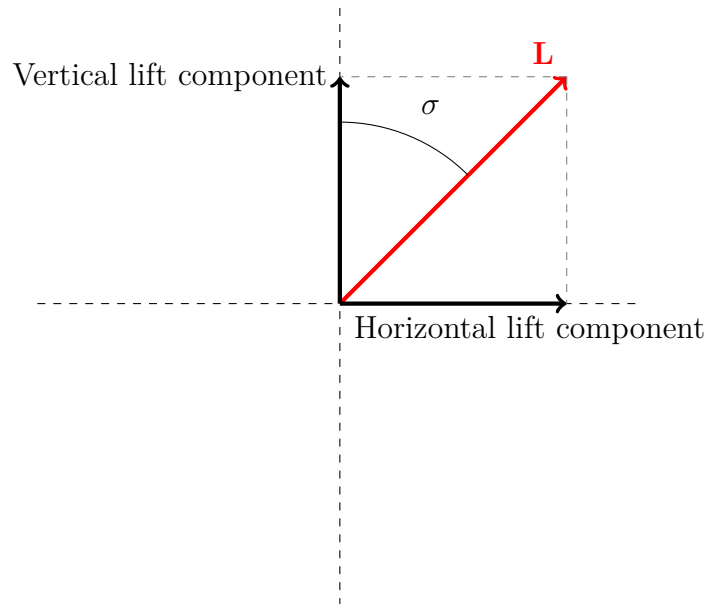


Figure 4.2: Bank angle

of its lift force, thereby influencing its trajectory. This technique is referred to as bank angle modulation, Figure 4.3.

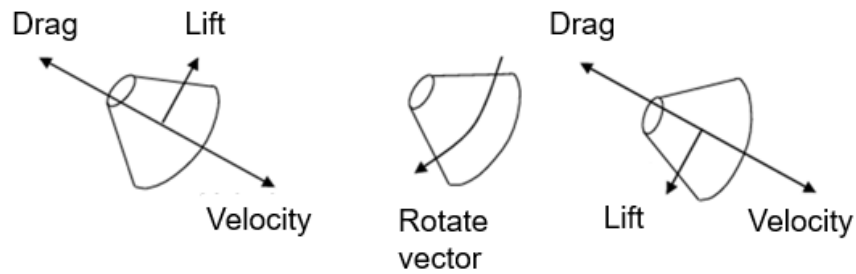


Figure 4.3: Bank angle modulation

A vehicle with a nonzero lift-to-drag (L/D) ratio can utilize bank angle modulation to regulate the lift force. The aerodynamic drag force always acts opposite to the velocity vector, while the lift force direction depends on the vehicle's orientation relative to the airflow.

When the bank angle is 0° , the lift vector points upward, creating a "full-lift up" condition that maximizes the travel distance. Conversely, a bank angle of 180° directs the lift vector downward, resulting in a "full-lift down" condition and minimizing the distance traveled. Intermediate bank angles orient the lift vector laterally, causing the vehicle to deviate from the nominal trajectory plane. Consequently, bank angle modulation significantly impacts the spacecraft trajectory, even for capsules with low L/D ratios, enabling controlled targeting of the landing site.

4.2 Guidance Strategy

The guidance algorithm, as previously introduced, consists of a predictor and a corrector. The predictor receives the current ECEF state vector and the time as inputs, estimating the future trajectory. Its output serves as the input for the corrector, which computes and updates the bank angle command at each guidance cycle. These components are described in detail in the following sections.

The guidance algorithm developed consists of three main phases:

1. **Initial Entry:** From the first EIP until the atmospheric density increases enough to provide sufficient control authority. During this phase, the bank

angle is maintained constant in a full-lift-up condition.

2. **Skip:** Active when aerodynamic load is greater than 0.05 g. During this phase, the predictor-corrector operates and a bank angle is commanded at each guidance cycle. If a skip maneuver is not possible or not necessary direct entry occurs.
3. **Ballistic:** This phase begins at atmospheric exit and continues until the second EIP in the case of a skip entry trajectory. When the g-load is lower than 0.05 g, the bank angle remains constant at the last computed value due to the low atmospheric density, which significantly limits control authority.

In Figure 4.4 the guidance algorithm and its transition logic is schematized.

The longitudinal and lateral dynamics are decoupled, assuming minimal cross-track errors, with lateral guidance achieved through periodic bank reversals.

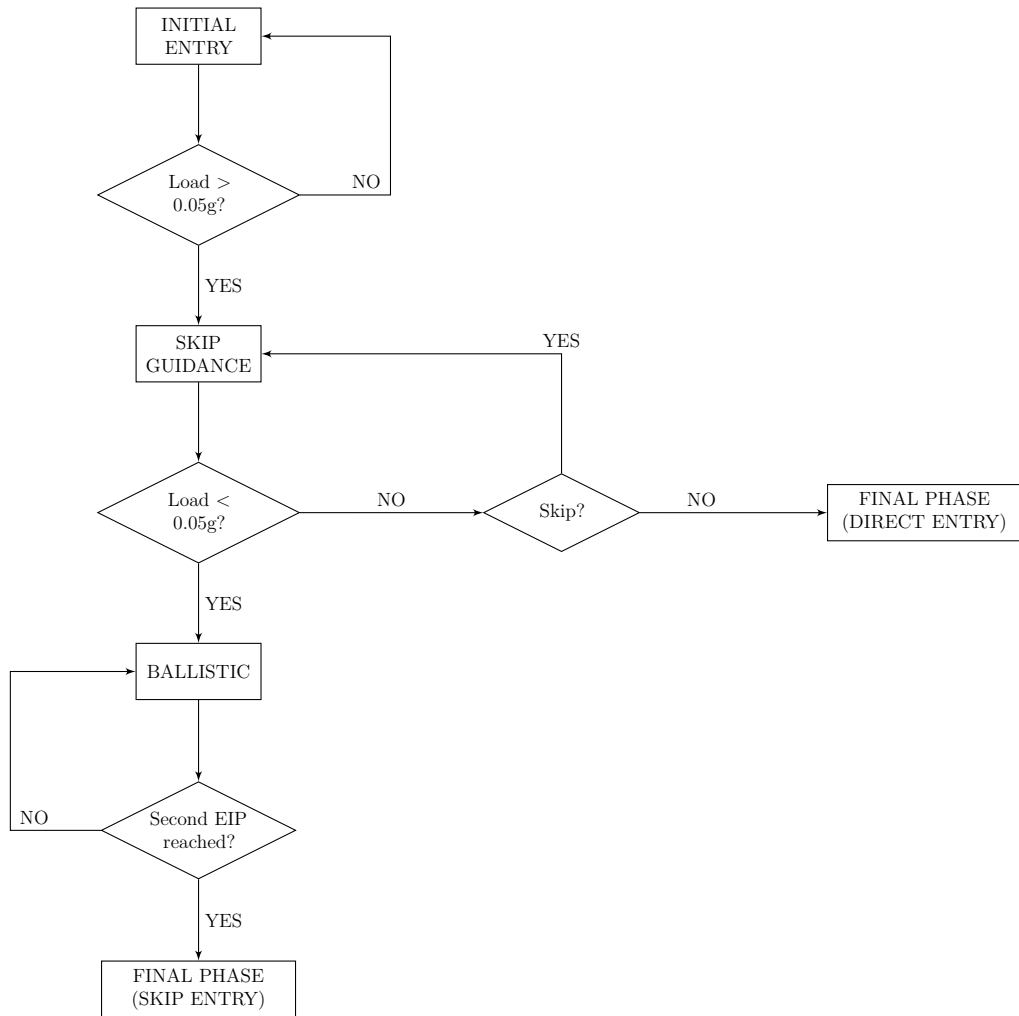


Figure 4.4: Guidance algorithm flowchart

4.2.1 Longitudinal Guidance

The longitudinal guidance controls the spacecraft trajectory in terms of downrange, ensuring that it reaches the desired target. This aspect of guidance focuses on adjusting the vehicle trajectory to achieve the correct distance traveled over the Earth surface.

As mentioned before, a Numerical Predictor-Corrector method (Figure 4.5) is employed to manage the longitudinal guidance. This approach enables precise control over the re-entry path, compensating for dynamic variations encountered during atmospheric re-entry.

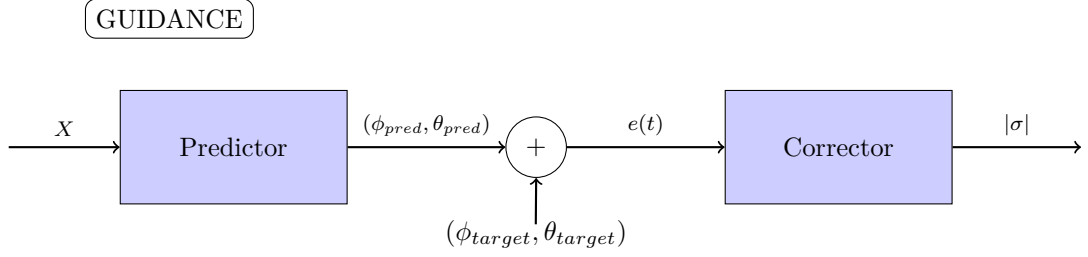


Figure 4.5: Guidance block scheme

Predictor

The predictor consist of a propagator that estimates the spacecraft trajectory from the current ECEF state (\mathbf{x}) to the target, which is defined in terms of latitude and longitude at an altitude of 120 km, corresponding to the second EIP.

It integrates the equations of motion in an Earth-Centered Inertial (ECI) Cartesian reference frame using a fourth-order Runge-Kutta method with a fixed integration step of 1s. Throughout the propagation, the bank angle remains constant at the value determined in the previous cycle.

The predictor outputs the predicted coordinates of the second EIP in terms of latitude ϕ_{pred} and longitude θ_{pred} . Subsequently, the predicted downrange d_{pred} , i.e., the distance from the current position to the predicted final position, is computed as:

$$d_{pred} = R_E \cos^{-1} (\sin \phi_0 \sin \phi_{pred} + \cos \phi_0 \cos \phi_{pred} \cos(\theta_{pred} - \theta_0)) \quad (4.2)$$

where,

- R_E : medium Earth radius,
- ϕ_0, θ_0 : current latitude and longitude,
- $\phi_{pred}, \theta_{pred}$: Predicted final point latitude and longitude.

Simultaneously, the desired downrange d_{des} , representing the distance from the current position to the target, is determined:

$$d_{des} = R_E \cos^{-1} (\sin \phi_0 \sin \phi_{target} + \cos \phi_0 \cos \phi_{target} \cos(\theta_{target} - \theta_0)) \quad (4.3)$$

where,

- $\phi_{target}, \theta_{target}$: Target latitude and longitude.

Both distances are calculated using a great-circle arc formula, assuming a spherical Earth. The difference between the predicted and desired downrange serves as the error input to the corrector. It is calculated as:

$$e(t) = d_{pred} - d_{des} \quad (4.4)$$

Corrector

The corrector (Figure 4.6) implements a PID controller with the following expression:

$$w(t) = K_p e(t) + K_i \int e(t) dt + K_d \frac{de(t)}{dt} \quad (4.5)$$

where:

- $e(t)$ is the error between predicted and desired downrange,
- K_p, K_i and K_d are the proportional, integral, and derivative gains respectively.

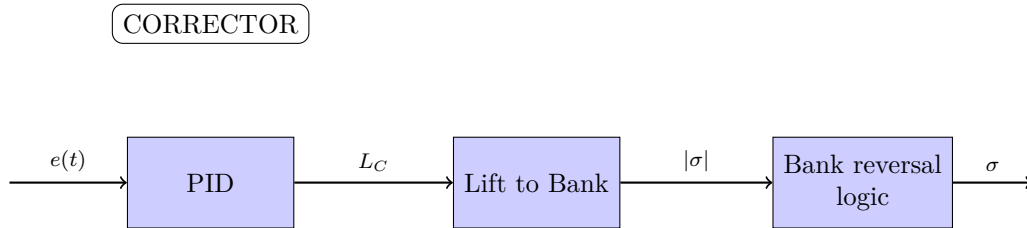


Figure 4.6: Corrector scheme

The output of the PID controller is the lift command L_c , which determines the commanded bank angle σ to be applied in the next cycle. The bank angle is computed using the following relation:

$$L_c = w(t) \quad (4.6.1)$$

$$|\sigma| = \cos^{-1} \left(\frac{L_c}{L} \right) \quad (4.6.2)$$

The process outlined, referred to as longitudinal logic, determines the magnitude of the bank angle required to adjust the vehicle trajectory in the longitudinal direction, in terms of downrange.

4.2.2 Lateral Guidance

For lateral control, ensuring correct latitude targeting, the bank reversal technique is employed and shown in Figure 4.7. This approach is essential for managing the cross-range trajectory of the spacecraft. The lateral guidance logic actively monitors the spacecraft's heading relative to the desired bearing.

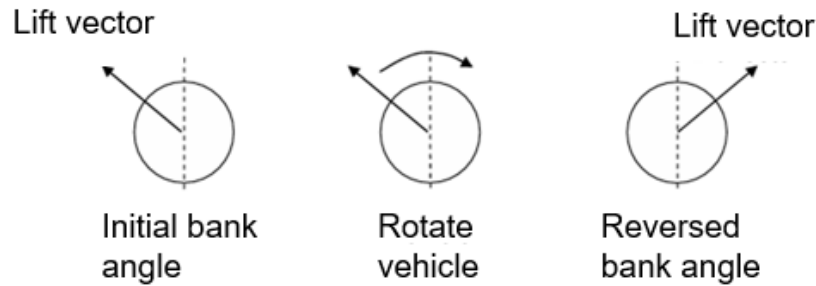


Figure 4.7: Bank reversal

The bank reversal strategy calculates the difference between the current heading and the target bearing (Figure 4.8) using the following relation:

$$\Delta\psi = \psi - \chi \quad (4.7)$$

where,

- ψ : Heading
- χ : Bearing
- $\Delta\psi$: Heading error

A threshold, known as the heading error limit ($\Delta\psi_{limit}$), is defined, and comparing these values determines the bank angle sign. If the heading error exceeds the threshold, a bank reversal is applied by inverting the previous bank angle sign.

$$\text{Sign}(\sigma) = \begin{cases} +1, & \text{if } \Delta\psi < \Delta\psi_{limit} \\ -1, & \text{if } \Delta\psi \geq \Delta\psi_{limit} \end{cases} \quad (4.8)$$

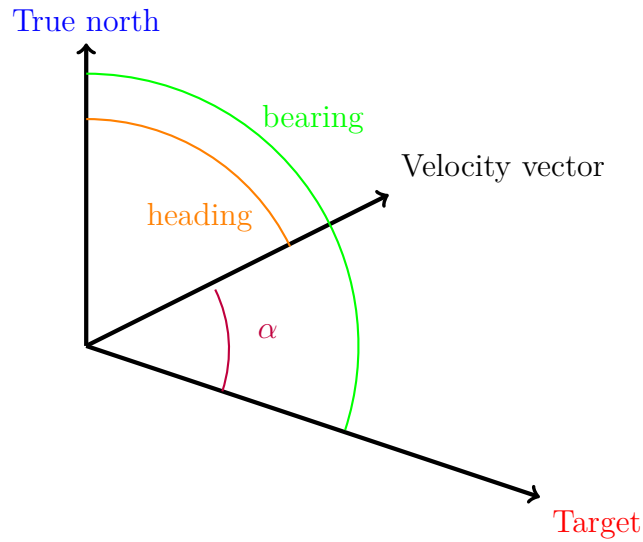


Figure 4.8: Heading error

This strategy ensures that the vehicle remains within the desired flight corridor.

Bank Angle Rate Limits

To ensure the physical feasibility of the maneuver, a constraint is applied to the variation of the bank angle per cycle. Instantaneous changes are not possible due to the spacecraft dynamic limitations. Therefore, the bank angle commanded by the PID controller is smoothed by limiting its rate of change to a predefined threshold per second, ensuring gradual and controlled adjustments.

4.3 Optimization

This study addresses an optimal control problem characterized by a set of control variables and boundary conditions. Given that the problem involves specific terms, such as the bank angle, which are defined through the subproblem detailed in the longitudinal guidance section, an advanced approach has been adopted. In particular, the problem has been tackled using efficient optimization techniques, including black-box optimization and a genetic algorithm, to effectively explore the solution space and identify optimal control strategies.

4.3.1 Mathematical model formulation

Optimal control theory is a branch of control theory that deals with finding a control for a dynamical system over a period of time such that an objective function is optimized (see e.g. [16]).

Here below are reported the general optimal control problem statement.

Functional to minimize/maximize:

$$J = \phi(\mathbf{x}_{(j-1)+}, \mathbf{x}_{j-}, t_{(j-1)+}, t_{j-}) \quad (4.9)$$

s.t.

$$\dot{\mathbf{x}}(t) = f[(\mathbf{x}(t), \mathbf{u}(t), t)] \quad (4.10)$$

$$\boldsymbol{\chi}(\mathbf{x}_{(j-1)+}, \mathbf{x}_{j-}, t_{(j-1)+}, t_{j-}) = \mathbf{0} \quad (4.11)$$

$$\mathbf{g}[(\mathbf{x}(t), \mathbf{u}(t), t)] \leq \mathbf{0} \quad (4.12)$$

In the case of this thesis Mayer's formulation has been adopted to express J .
Where,

- $\dot{\mathbf{x}} = f$ state equations,
- $\mathbf{x}(t)$ state variables,
- $\mathbf{u}(t)$ control variables,
- t independent variable,
- $(\mathbf{x}_{0+}, \mathbf{x}_{1-}), \dots, (\mathbf{x}_{(p-1)+}, \mathbf{x}_{p-})$ trajectory arcs,
- $\boldsymbol{\chi}$ boundary conditions,
- \mathbf{g} additional constraints.

In this specific case, the problem can be formulated as follow. The functional to minimize/maximize simply consists of calculating the error in the final position d_{error} .

It represent the magnitude of the distance between the final position $(\phi_{final}, \theta_{final})$ obtained as an outcome of the process, and the desired target position $(\phi_{target}, \theta_{target})$

This distance quantifies the deviation between the actual endpoint and the specified target location.

$$d_{error} = R_E \cos^{-1} (\sin \phi_{final} \sin \phi_{target} + \cos \phi_{final} \cos \phi_{target} \cos(\theta_{target} - \theta_{final})) \quad (4.13)$$

where,

- $\phi_{final}, \theta_{final}$: latitude and longitude at final time,
- $\phi_{target}, \theta_{target}$: Target latitude and longitude.

The specific state equations are represented by the equations of motion reported above in Equation 4.1 with an additional equation introduced solely to enforce the constraint imposed on the bank angle rate, ensuring consistency with the general formulation. The modified state equations are given:

$$\left\{ \begin{array}{l} \dot{r} = V \sin \gamma \\ \dot{\theta} = \frac{V \cos \gamma \sin \psi}{r \cos \phi} \\ \dot{\phi} = \frac{V \cos \gamma \cos \psi}{r} \\ \dot{V} = -\frac{D}{m} - \frac{\sin \gamma}{r^2} + \Omega^2 r \cos \phi (\sin \gamma \cos \phi - \cos \gamma \sin \phi \cos \psi) \\ \dot{\gamma} = \frac{1}{V} \left[\frac{L \cos \sigma}{m} + \left(V^2 - \frac{1}{r} \right) \frac{\cos \gamma}{r} + 2\Omega V \cos \phi \sin \psi \right. \\ \quad \left. + \Omega^2 r \cos \phi (\cos \gamma \cos \phi + \sin \gamma \cos \psi \sin \phi) \right] \\ \dot{\psi} = \frac{1}{V} \left[\frac{L \sin \sigma}{m \cos \gamma} + \frac{V^2 r \cos \gamma \sin \psi \tan \phi}{r} - 2\Omega V (\tan \gamma \cos \psi \cos \phi - \sin \phi) \right. \\ \quad \left. + \frac{\Omega^2 r \sin \psi \sin \phi \cos \phi}{\cos \gamma} \right] \\ \dot{\sigma} = \hat{\sigma} \end{array} \right. \quad (4.14)$$

As a consequence the state vector turns out to be as follow:

$$\hat{\mathbf{x}}(t) = [r(t), \phi(t), \theta(t), V(t), \gamma(t), \psi(t), \sigma(t)]^T$$

The bank angle is assumed as in Equation 4.6.2, where L_c is defined as in Equation 4.5.

The PID gains K_p , K_i and K_d , can be assumed as control parameters. The following initial condition are given:

$$\begin{cases} r(0) = r_0, \\ \phi(0) = \phi_0 \\ \theta(0) = \theta_0 \\ V(0) = V_0 \end{cases} \quad (4.15)$$

Additionally, γ_0 and ψ_0 , the flight path angle and the heading angle at the first atmospheric entry, are initial conditions unknown and to be determined.

The control parameters vector is reported:

$$\mathbf{u} = [K_p, K_i, K_d]^T$$

An additional constraint is applied to the magnitude of the bank rate, therefore the derivative of the bank angle have to be below the maximum admissible bank rate, S_{max} :

$$|\dot{\sigma}| \leq S_{max} \quad (4.16)$$

It can be noticed that the magnitude of the bank angle $|\sigma|$ depends directly on the control parameters K_p, K_i, K_d .

4.3.2 Numerical approach

Given the complexity of the problem, a combined approach integrating black-box optimization and a genetic algorithm has been adopted. The use of black-box optimization is motivated by the fact that σ directly depends on an extensive computational process, as outlined in subsection 4.2.1. The genetic algorithm has been employed to enhance the global search capability, as discussed in Appendix B.

The simulator solves the equations of motion using a fourth-order Runge-Kutta integration method. Black Box approach are dealt with in depth in Appendix A. In Figure 4.9 are reported a schematic illustration of the BBO utilized. Where $\dot{\mathbf{x}}$ as in Equation 4.14

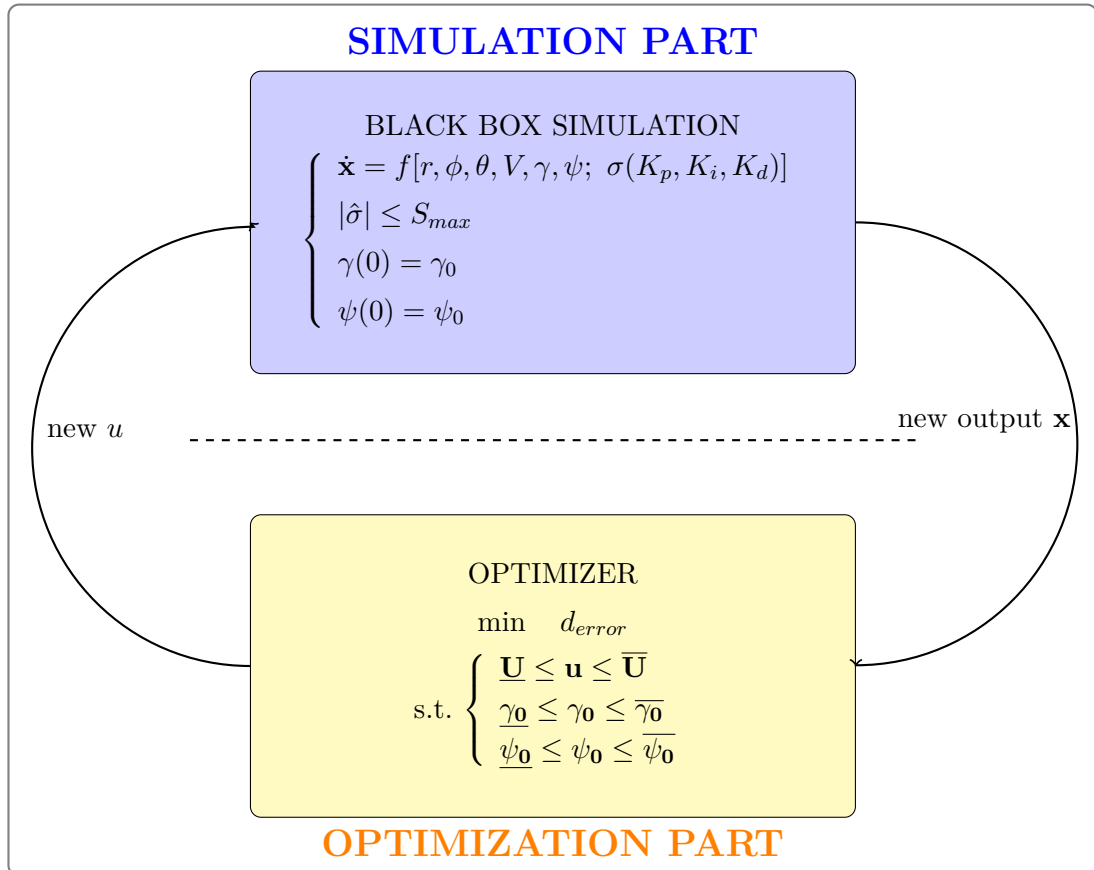


Figure 4.9: Black Box Optimization scheme

Chapter 5

Experimental analysis

The simulation model developed for the re-entry scenario under study is illustrated in Figure 5.1. The aim is to guide a vehicle returning from the Moon to Earth, starting at the first EIP at 120km of altitude and ending at the second EIP (also at 120km), executing a skip maneuver in between. The simulation terminates once the vehicle completes the skip and returns to 120km of altitude.

The model has been implemented in Simulink using the ODE4 solver with a fixed time step of 0.1s. The guidance block operates as a triggered subsystem, updating its outputs at a frequency of 1Hz. The simulation model consists of three main blocks:

1. **Environmental block:** This block calculates the atmospheric density and gravitational acceleration at each time step, using $r(t)$ — the distance from the Earth's center — as an input.
2. **Motion equations block:** This block integrates the equations of motion (as described in 4.1.1), using density, gravitational acceleration, and the current bank angle. It outputs the state vector $\mathbf{x}(t)$ in the ECEF reference frame.
3. **Guidance block:** This block receives the state vector $\mathbf{x}(t)$ from the motion equations block and computes a new bank angle every 1s.

These three blocks operate together to simulate the skip re-entry trajectory from the first EIP (Table 5.1) to the second EIP (Table 5.2) , generating as output the vehicle's trajectory, the time history of the state vector, and key flight parameters such as altitude, velocity, and bank angle variations throughout the maneuver.

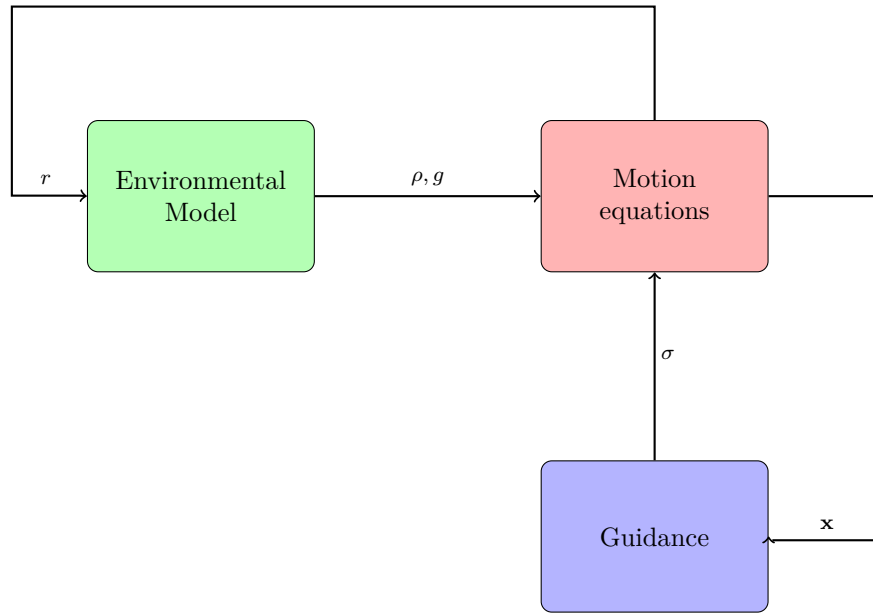


Figure 5.1: Simulation model scheme

where,

- r : radial distance from the Earth center ,
- ρ : atmospheric density,
- g : gravitational acceleration,
- \mathbf{x} : ECEF state vector,
- σ : bank angle

5.1 Mission Scenario

The mission scenario analysed in this study is described in this section. As briefly mentioned in advance, the vehicle trajectory starts at the first EIP (Table 5.1), where the value of altitude, latitude, longitude, velocity and bank angle, are imposed, while the flight path angle and heading angle are obtained from the optimization process detailed in section 4.3. The target point to be reached is imposed in terms of altitude, latitude and longitude (Table 5.2).

Parameter	Value
Altitude h_0	120 km
Latitude ϕ_0	-33.4°
Longitude θ_0	-160.0°
Velocity V_0	10654 m/s
Flight path angle γ_0	-5.77°
Heading angle ψ_0	77.4°
Bank angle σ_0	0°

Table 5.1: First EIP

Parameter	Value
Altitude h_{target}	120 km
Latitude ϕ_{target}	30.0°
Longitude θ_{target}	-52.8°

Table 5.2: Second EIP

The specific aerodynamic parameters of the vehicle under consideration are given in Table 5.3, highlighting a low L/D value.

Parameter	Value
Lift-to-Drag ratio L/D	0.15
Lift coefficient C_L	0.207
Drag coefficient C_D	1.38

Table 5.3: Aerodynamic properties

The threshold value, designated as the "limit", for executing a bank reversal is set to 0.1° (subsection 4.2.2).

In consideration of the mission scenario that has been selected and described, the optimal control problem has been resolved, resulting in the establishment of the initial values for γ_0 and ψ_0 , which are reported in Table 5.1. The gains of the PID controller, which have been determined through this process, are also specified in Table 5.4.

Parameter	Value
K_p	4.0784e-2
K_i	9.6298e-2
K_d	0.4848e-2

Table 5.4: Chosen PID controller gains

Constraints

1. Maximum bank rate: the bank angle can vary at a maximum rate, in this case set at 15 degrees/second. This limitation is due to the fact that actuators have physical limits on the speed at which they can operate, and a too rapid change could cause instability in the aerodynamic configuration of the vehicle or generate sudden forces that increase the load on the structure.
2. Maximum G-Load: to preserve the structural integrity of the vehicle during re-entry, the g-load must remain within safe operational limits, ensuring it does not exceed the structure's tolerance.
3. Maximum heat flux: the thermal load must remain below the critical threshold to prevent material degradation, with an additional safety margin to account for uncertainties and variations in the re-entry conditions.

Of the above constraints, only the maximum bank angle rate constraint is explicitly imposed in the developed simulation model. The G-load and heat flux constraints are checked downstream of the analysis.

5.1.1 Results

The results obtained for the scenario described in section 5.1 are reported herein below. The entire skip entry phase, for this scenario, lasts 1800 seconds, equivalent to 30 minutes. In Figure 5.2 is reported the trajectory profile for the defined mission scenario.

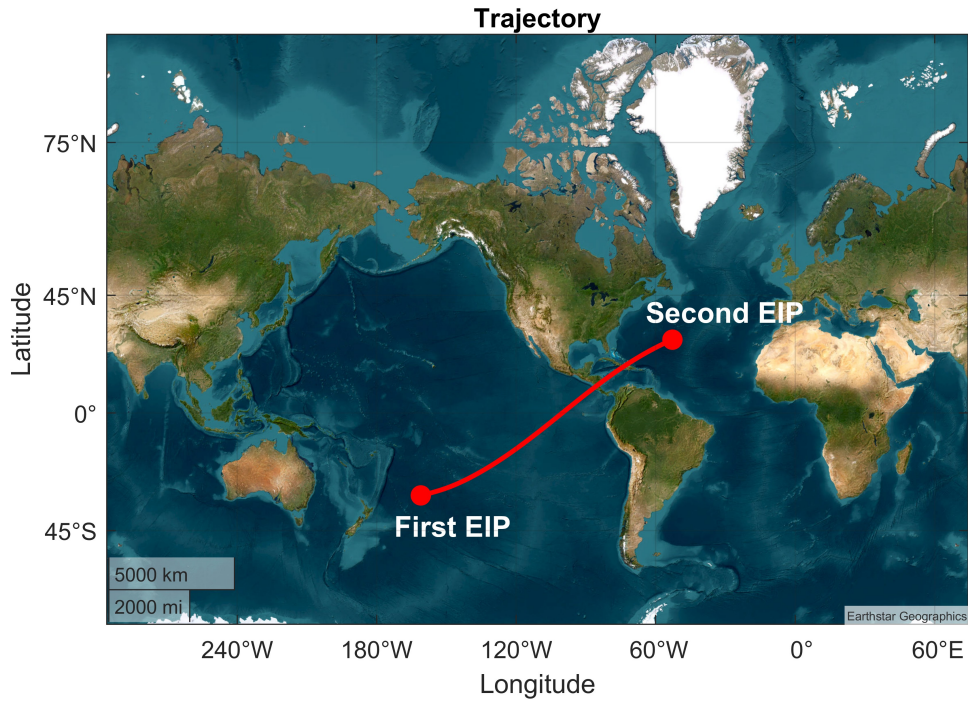


Figure 5.2: Trajectory profile

In Figure 5.3 the vehicle trajectory is reported in terms of altitude-range, while in Figure 5.4 the values of latitude and longitude assumed during the trajectory are shown.

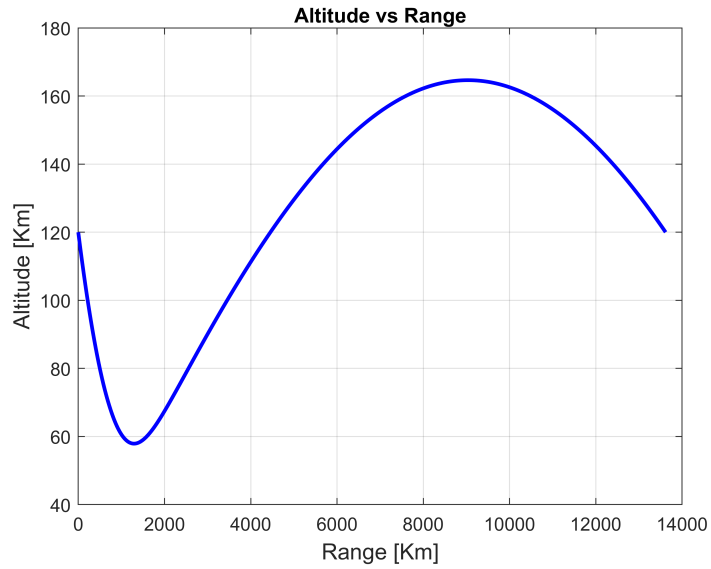


Figure 5.3: Altitude vs Range

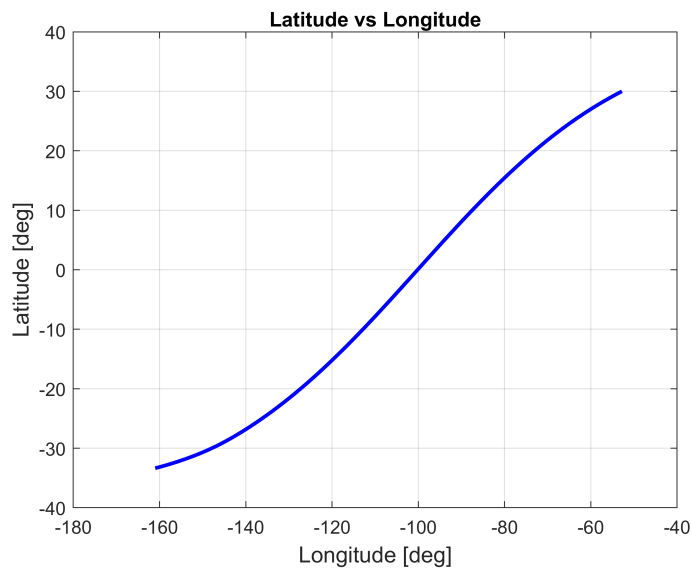


Figure 5.4: Latitude vs Longitude

In Figure 5.5 the values assumed by circular velocity can be seen over time. Note that the largest part of the velocity is lost in the first 200s, which, as shown in Figure 5.6 corresponds to the part of the trajectory performed at the lowest altitude.

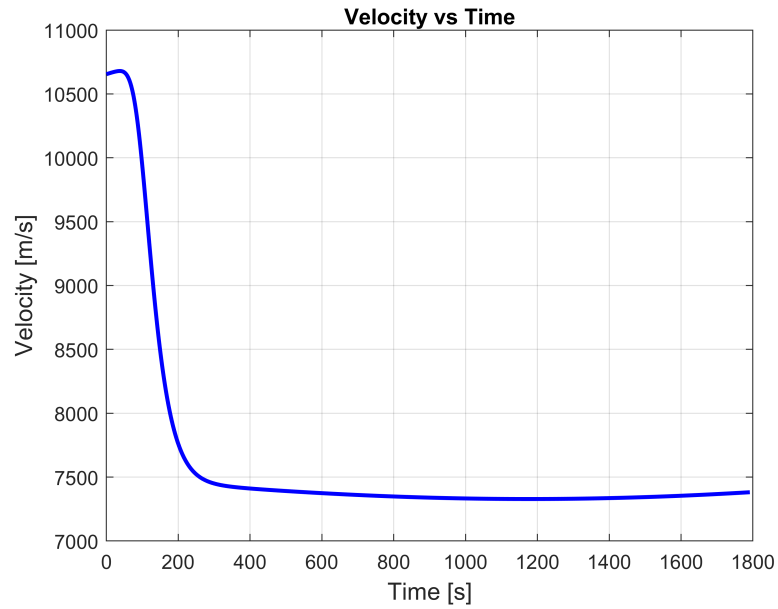


Figure 5.5: Velocity vs Time

In Figure 5.6, initially, both velocity and altitude decrease rapidly, followed by a keplerian phase where altitude increases again. In this phase, the trajectory exhibits overlapping ascent and descent branches: the vehicle decelerates while climbing and accelerates while descending. The first Entry Interface Point (EIP) appears on the right side of the graph, as it corresponds to higher velocities.

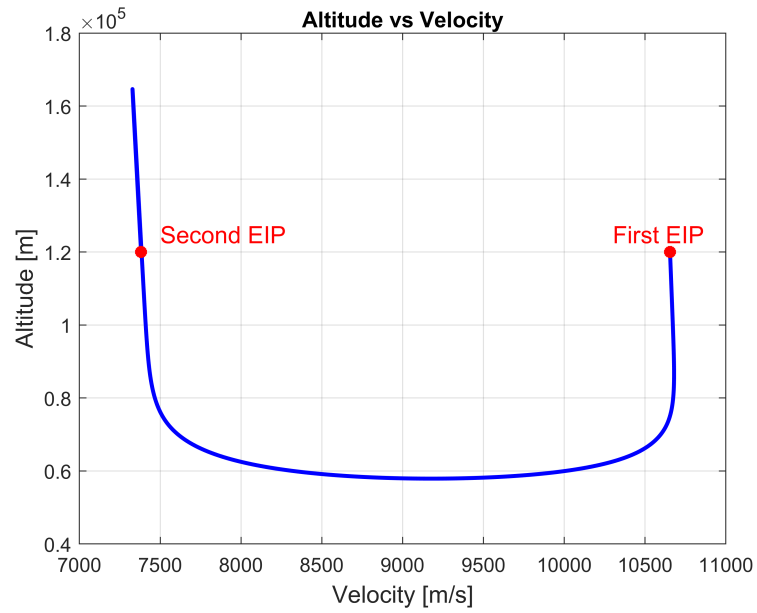


Figure 5.6: Altitude vs Velocity

Figure 5.7 and Figure 5.8 show the trends of the flight-path angle and the heading angle respectively.

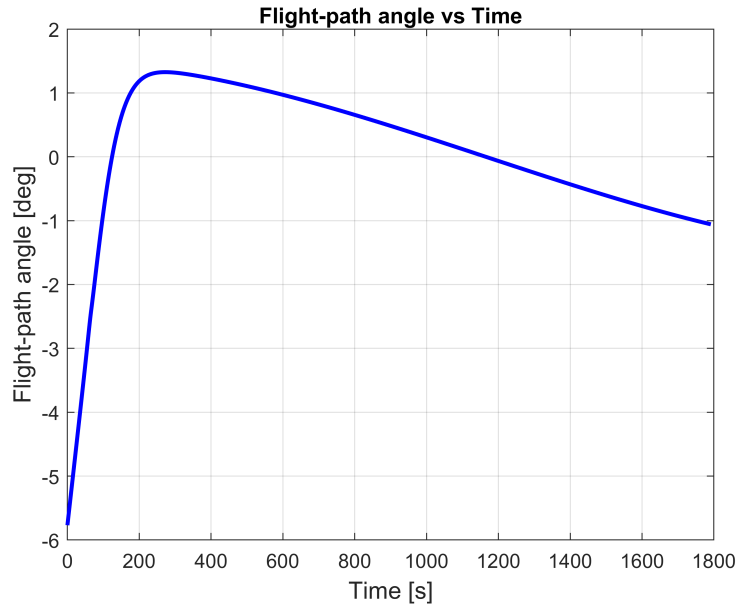


Figure 5.7: Flight path angle vs Time

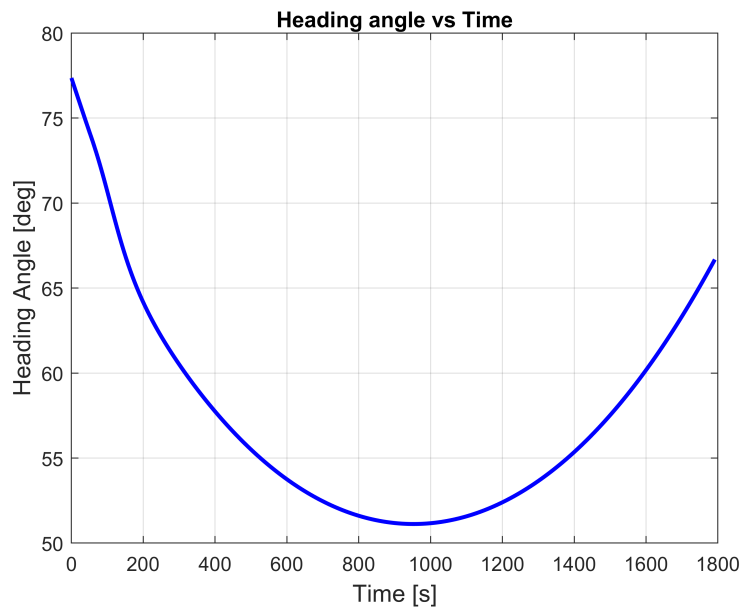


Figure 5.8: Heading angle vs Time

The bank angle profile reported in Figure 5.9 shows a constant value of 0° imposed as an initial condition, constant until the skip guidance takes control. At this point the skip will command the bank angle while the g-load is sufficient to ensure control authority. When the skip is executed and the vehicle exits the atmosphere, the vehicle maneuvers to the last accepted value and keeps it constant, in this case around 90° . This is a characteristic value because in this state the vertical lift component is almost zero and a minimal variation in bank angle will cause a variation, positive or negative, in the downrange. Two complete bank reversals are performed in order to follow as closely as possible the given heading corridor.

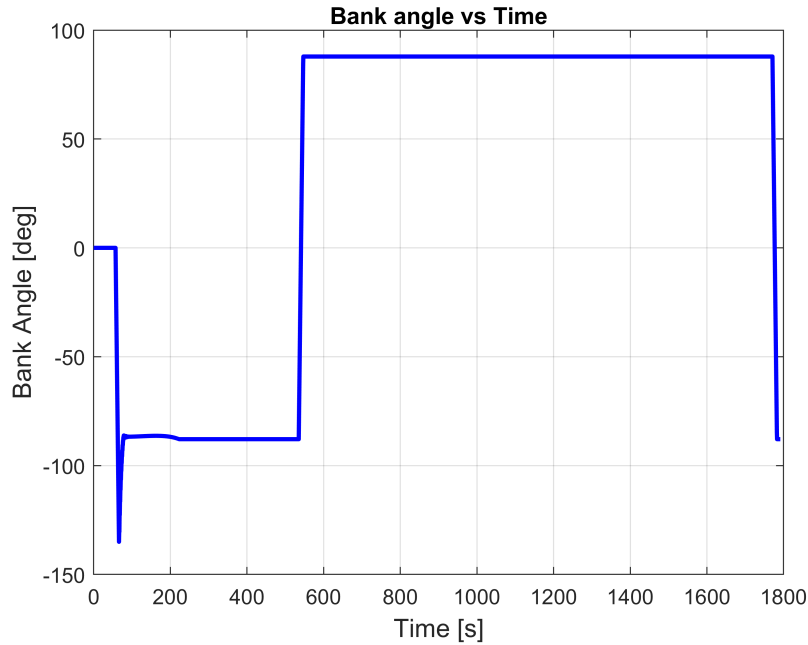


Figure 5.9: Bank angle vs Time

Peak values of dynamic pressure (Figure 5.10), G load (Figure 5.11) and heat flux (Figure 5.12) are reached corresponding to the lowest altitudes, as expected. All these peaks are well below the acceptable limits, therefore there are no structural problems. In Figure 5.13 the time evolution of the heat load is depicted, representing the integral of the heat flux over time. After a rapid initial increase, the heat load approaches an asymptote, indicating that once the peak is reached, the heat flux becomes negligible.

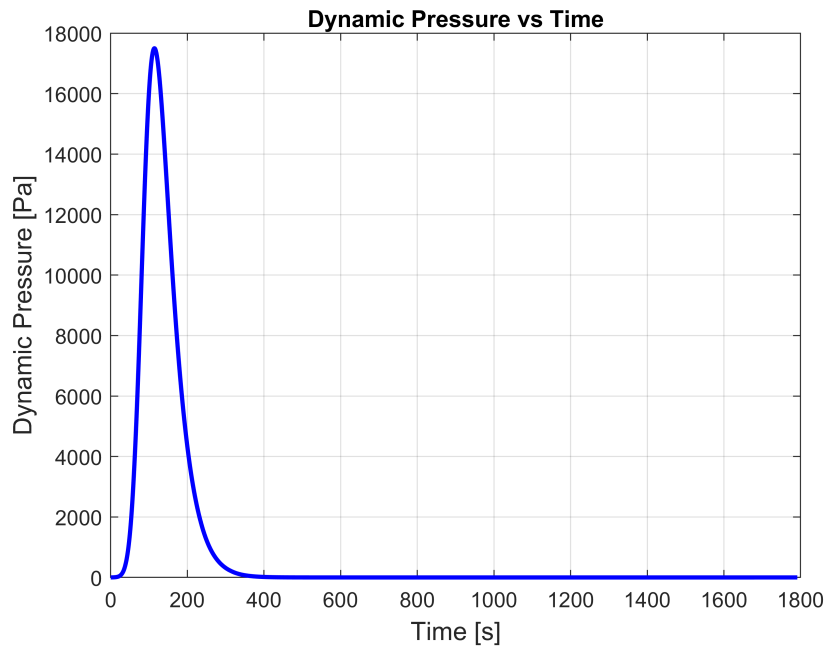


Figure 5.10: Dynamic pressure vs Time

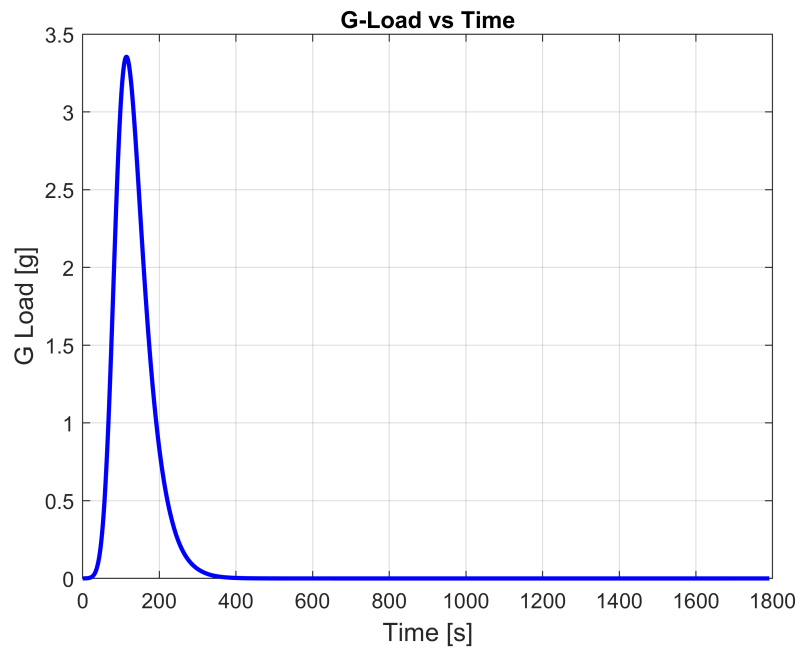


Figure 5.11: G-Load vs Time

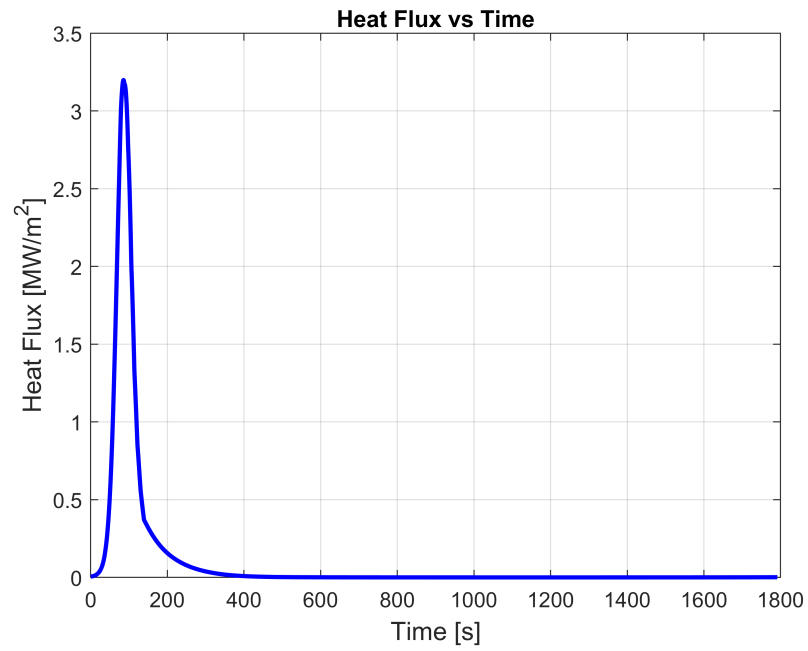


Figure 5.12: Heat flux vs Time

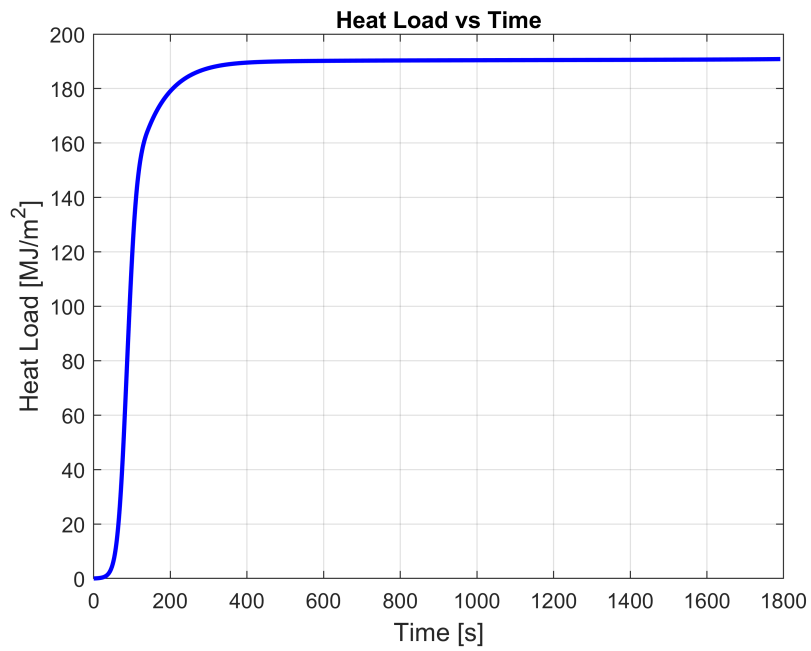


Figure 5.13: Heat load vs Time

Figure 5.14 shows the range error over time, i.e., the PID controller input, as calculated in Equation 4.4. An initial overshoot can be observed, followed by some oscillations and a rapid convergence. In general, PID convergence is not inherently guaranteed; however, in this case, optimization aids in achieving convergence close to zero. The range error, being a signed value, provides insights into whether the down-range is short or long, serving as crucial information for the corrector.

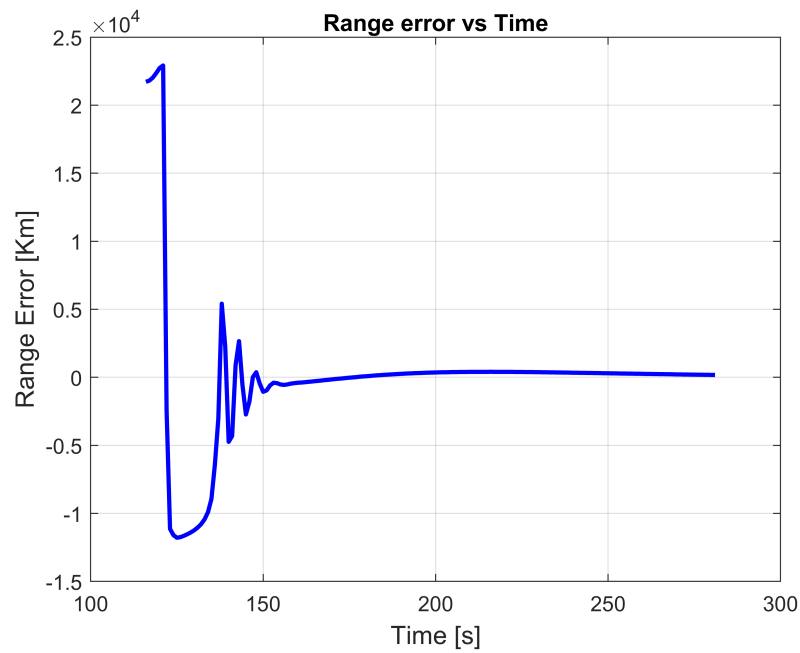


Figure 5.14: Range error vs Time

Instead, Figure 5.15 shows the trend of the distance to the targeted second EIP, calculated as Equation 4.13. It shows some oscillations as it decreases, but converges to zero in less than 100s from the beginning of the skip guidance.

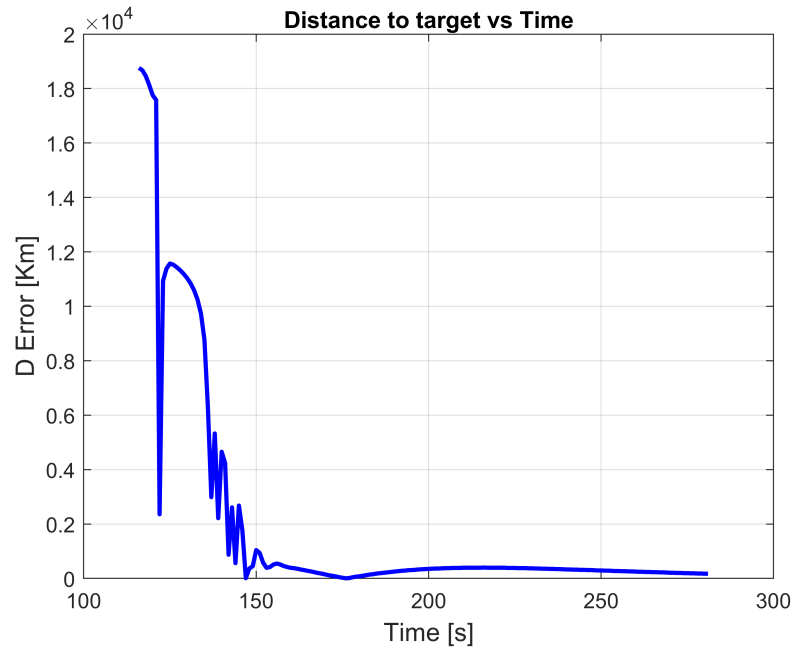


Figure 5.15: Distance from target vs Time

In this optimized scenario, the target is reached with a very high level of accuracy. The distance between the final position obtained from the simulation and the imposed target position is approximately 0.9 km, calculated as Equation 4.13 (Figure 5.16).

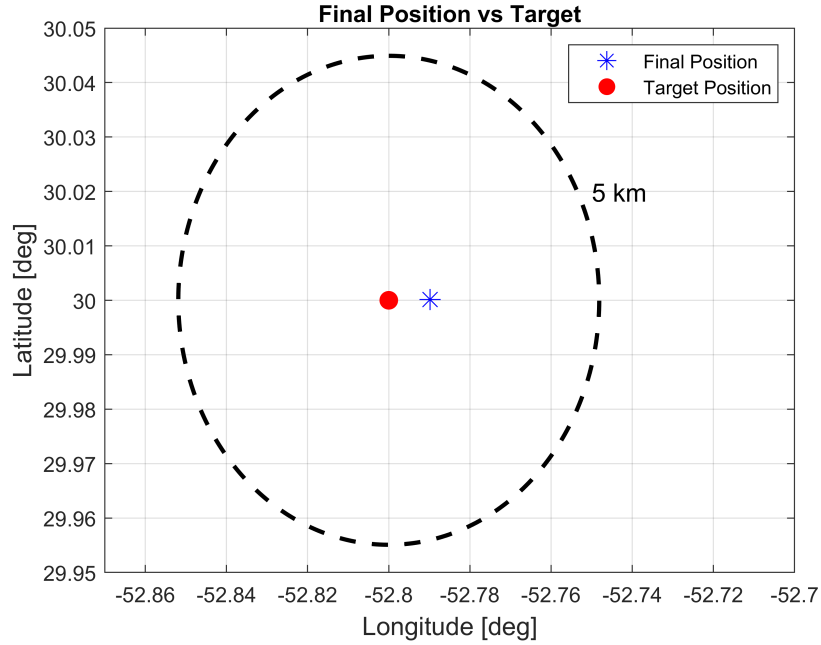


Figure 5.16: Final position vs Target position

5.2 Monte Carlo Analysis

The **Monte Carlo analysis** was conducted to assess the robustness of the algorithm in the presence of uncertainties in the system parameters. A total of 1000 simulations were performed, introducing variations in EIP conditions, atmospheric conditions, vehicle mass, and aerodynamic parameters.

- **EIP conditions:** Variations were introduced using a multivariate normal distribution, considering a covariance matrix to account for the dependencies among the state vector \mathbf{x} components.
- **Atmospheric conditions:** Atmospheric density was perturbed using a normal distribution applied to a reference dataset containing: density, altitude

and $1 - \sigma$ density. Therefore, for each altitude value, a $\rho_{perturbated}$ value was calculated as follows:

$$\rho(h) = \rho_{nominal}(h) \cdot (1 + \Delta\rho(h) \cdot randn) \quad (5.1)$$

where the rand value is a standard normally distributed random variable.

- **Vehicle mass:** Perturbed using a uniform distribution around the nominal value, considering a variation of $\pm 10\%$ of the nominal value.

$$m = m_{nominal} + \Delta m \cdot 2(rand - 0.5) \quad (5.2)$$

where rand is a uniform random variable in $[0,1]$ ensuring symmetric variations around the nominal value.

- **Aerodynamic parameters:** The L/D was perturbed with a uniform distribution within $\pm 10\%$ of its nominal value while ensuring consistency between the lift coefficient C_L and the drag coefficient C_D :

$$L/D = L/D_{nominal}(1 + 0.1 \cdot 2 \cdot (rand - 0.5)) \quad (5.3)$$

$$C_L = C_{L_{nominal}}(1 + 0.1 \cdot 2 \cdot (rand - 0.5)) \quad (5.4)$$

$$C_D = \frac{C_L}{L/D} \quad (5.5)$$

The dispersions described above are summarized in Table 5.5.

Parameters	Dispersion	3 - σ or min/max
$\Delta\rho$ (kg/m ³)	Gaussian	Tabulated varying with altitude
Δm (kg)	Uniform	$\pm 10\%$
L/D	Uniform	$\pm 10\%$
ΔC_L	Uniform	$\pm 10\%$
x		Covariance matrix

Table 5.5: Monte Carlo Parameter dispersions

5.2.1 Mission scenario results

This section shows the results of the Monte Carlo analysis performed as described in section 5.2. In Figure 5.17 are shown the final positions of 1000 different cases in terms of latitude and longitude. It can be seen that there are some points so far away from the chosen target that they can be considered as outliers. In particular, it was found that 98.9% of the analysed cases were acceptable. Therefore, in Figure 5.18, a refined version of the final position distribution is reported, removing the outliers to better evaluate the solution. It is important to note that, in the case of this study, a range error of approximately 200km from target is considered acceptable. This is due to the vehicle limited control authority, resulting from its aerodynamic characteristics. However, during the final phase of entry, the vehicle could correct errors of this magnitude and reach the designed landing site.

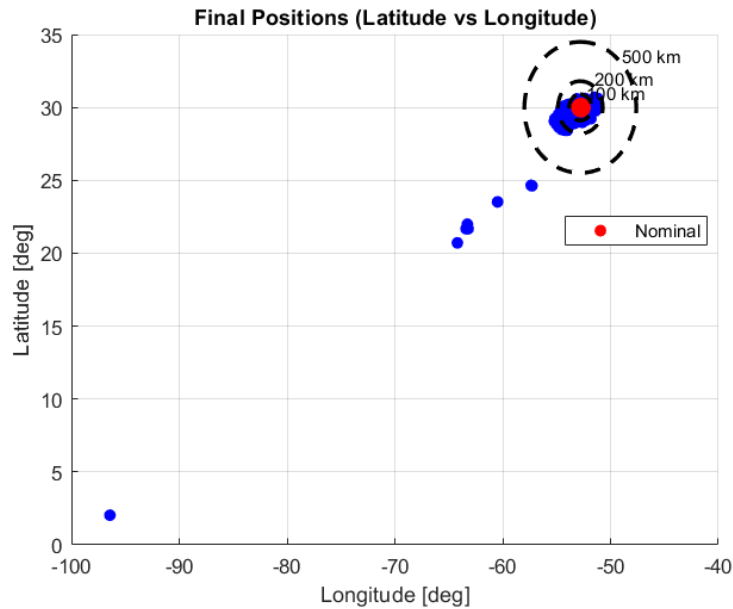


Figure 5.17: Distribution of final Positions (complete version)

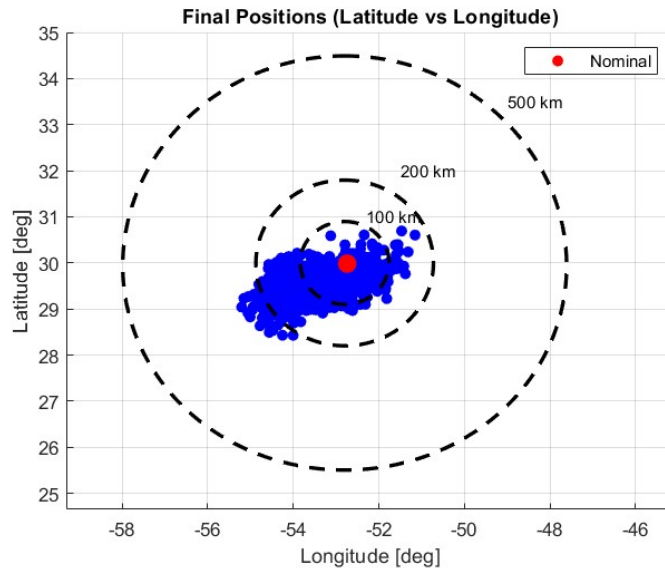


Figure 5.18: Distribution of final Positions (refined version)

All subsequent graphs have undergone a filtration process aimed at removing outliers to better highlight the trend of the various results. However, outlier cases have been analyzed separately and are discussed in the following sections.

Below in Figure 5.19 is the trajectory followed in terms of altitude - range.

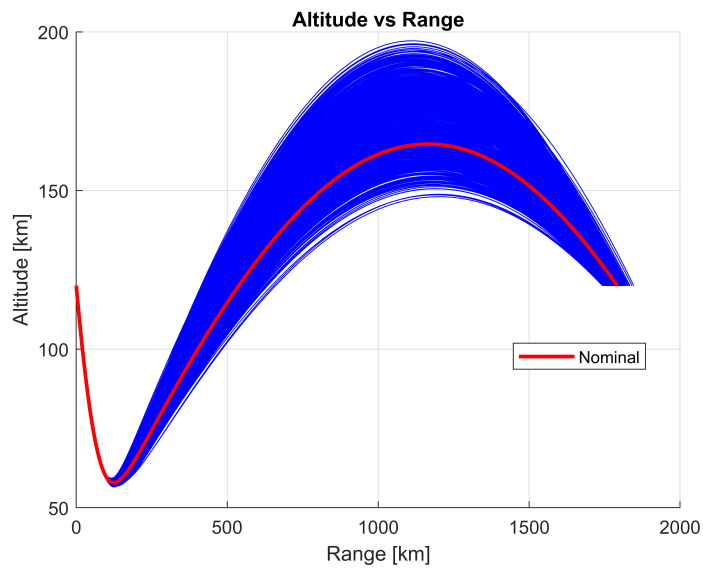


Figure 5.19: Altitude vs Range

In Figure 5.20 and in Figure 5.21 it is clear that the velocity does not present any evident deviation from the nominal case.

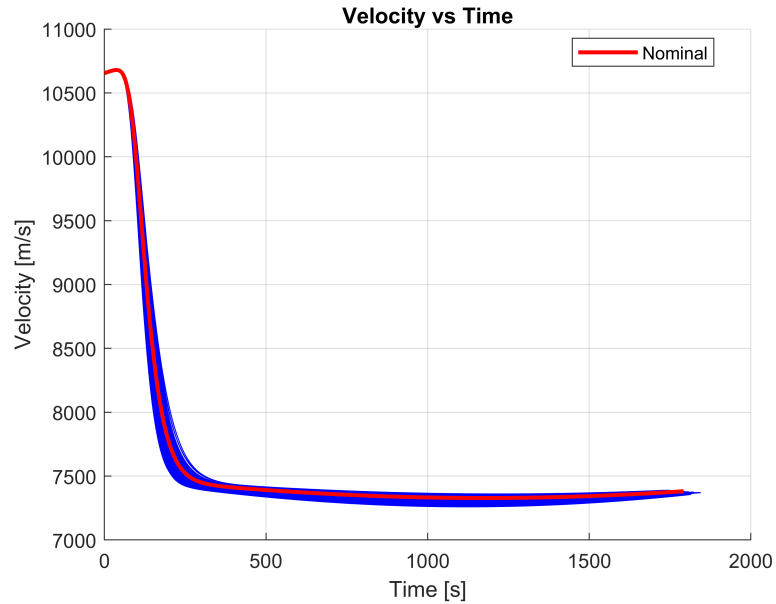


Figure 5.20: Velocity vs Time

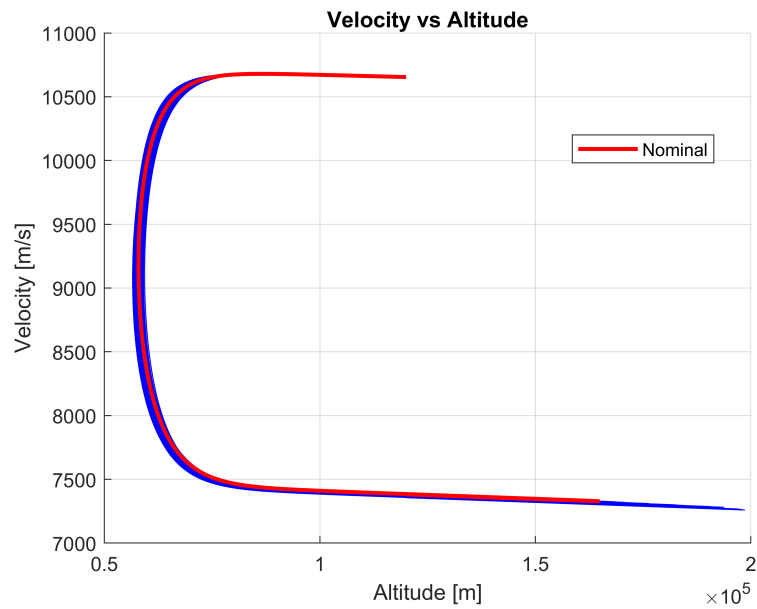


Figure 5.21: Altitude vs Velocity

In Figure 5.22 and Figure 5.23 the tendency of the flight-path angle and heading to follow the nominal case is highlighted .

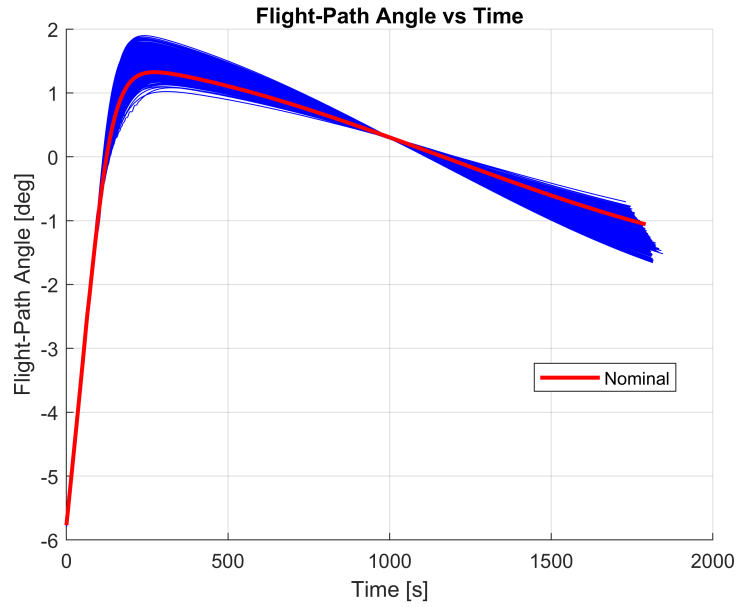


Figure 5.22: Flight-path angle vs Time

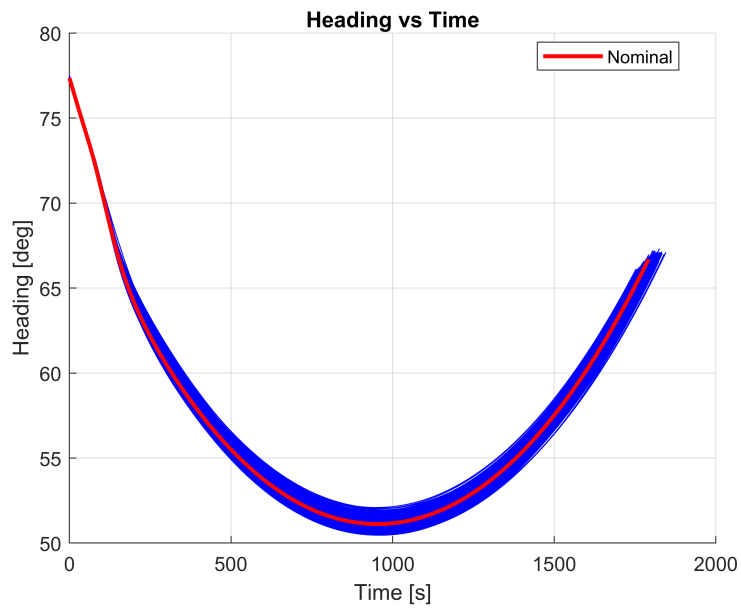


Figure 5.23: Heading vs Time

In Figure 5.24, which shows the density trends in the cases analysed, a significant deviation of the density values from the nominal value can be seen at low altitudes.

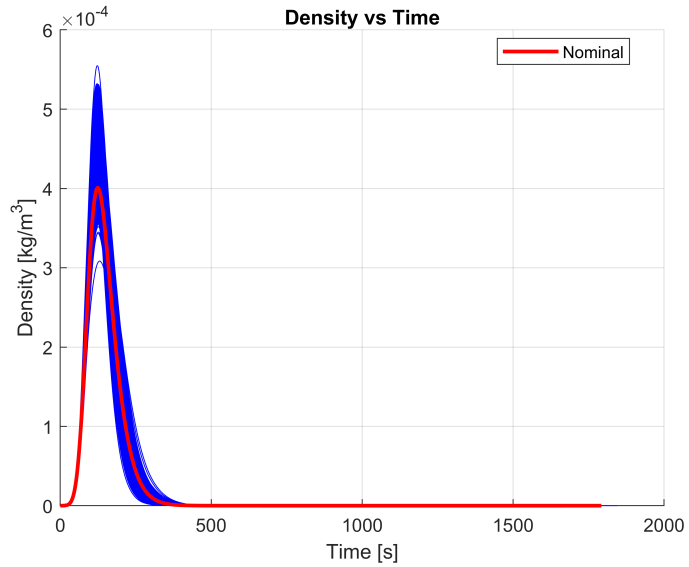


Figure 5.24: Density vs Time

In Figure 5.25, are reported bank angle profiles assumed.

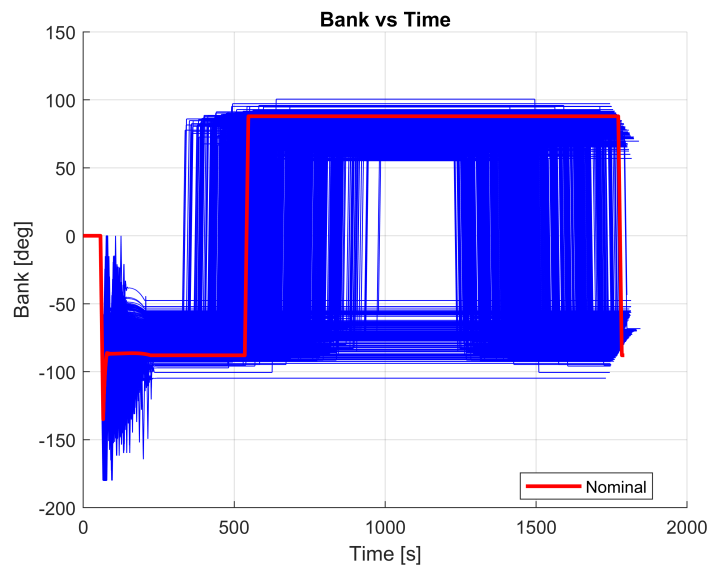


Figure 5.25: Bank angle vs Time

In Figure 5.26, Figure 5.27 , Figure 5.28 and Figure 5.29 the dynamic pressure, g-load, heat flux and heat load are presented in different scenarios. In all cases, the peak value remains within acceptable structural limits.

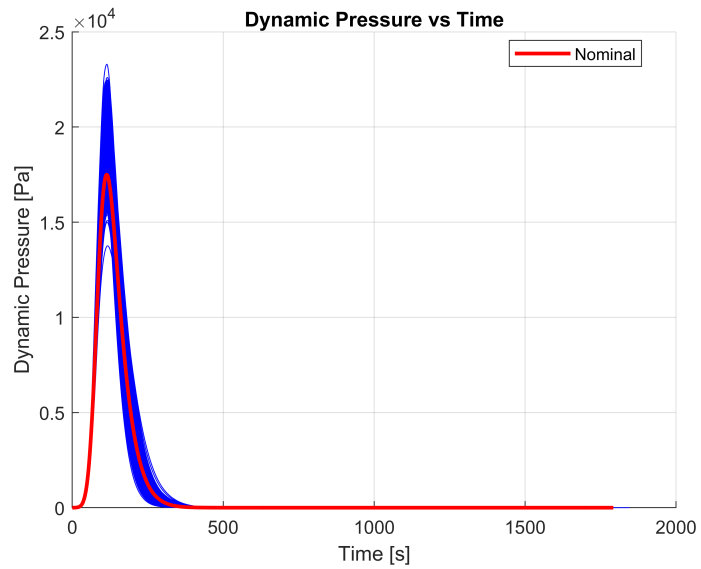


Figure 5.26: Dynamic pressure vs Time

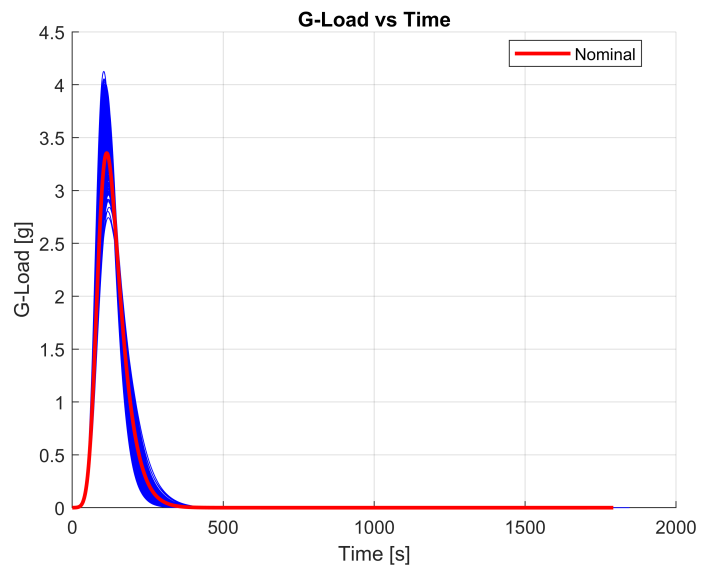


Figure 5.27: G-Load vs Time

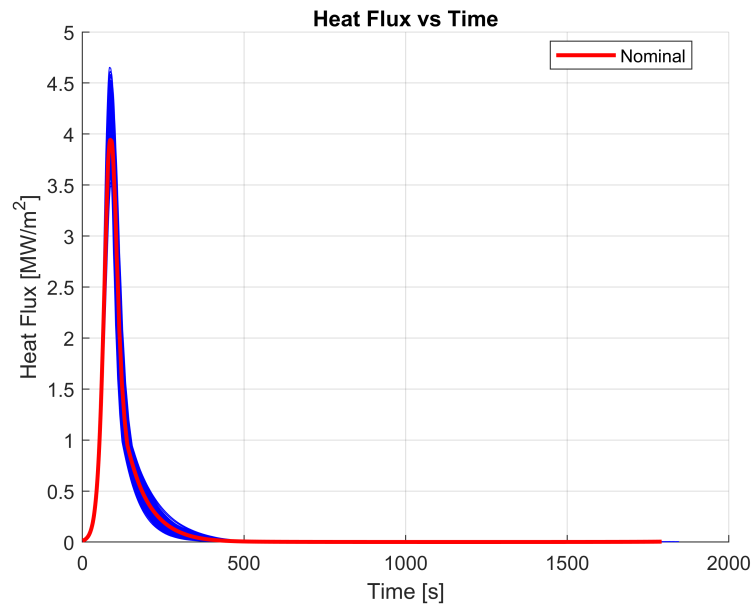


Figure 5.28: Heat flux vs Time

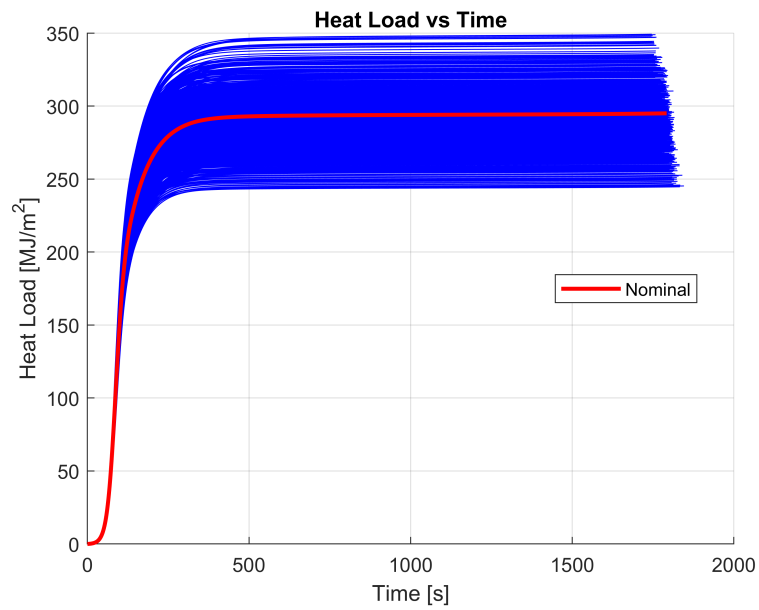


Figure 5.29: Heat load vs Time

In Figure 5.30 and Figure 5.31 the full and refined final positions are shown. Each point takes on a colour depending on its density trend. As explained in the legend, dark blue means very low density, while dark red means high density. These graphs are important to show a pattern in the solution distribution. It is important to note that the trajectories are strongly influenced by a low density atmosphere, which makes it difficult to control a low L/D vehicle due to the further reduced control authority. The outlier cases are characterised by very low density values combined with a low value of C_L , leading to difficult guidance. Also in the refined results in Figure 5.31 there is a pattern in the density values, low density tends to shorten the trajectory. The same zone is thickened in all cases with a similar density trend.

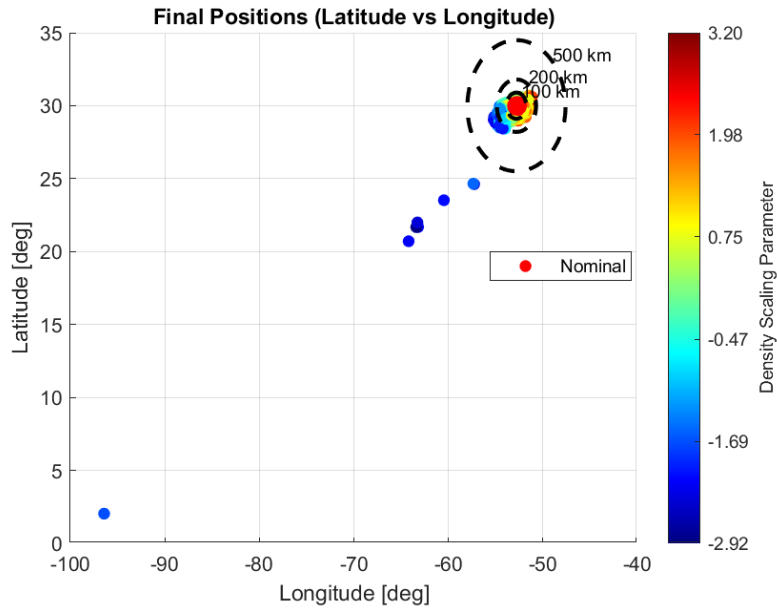


Figure 5.30: Distribution of final positions with density mapping (complete version)

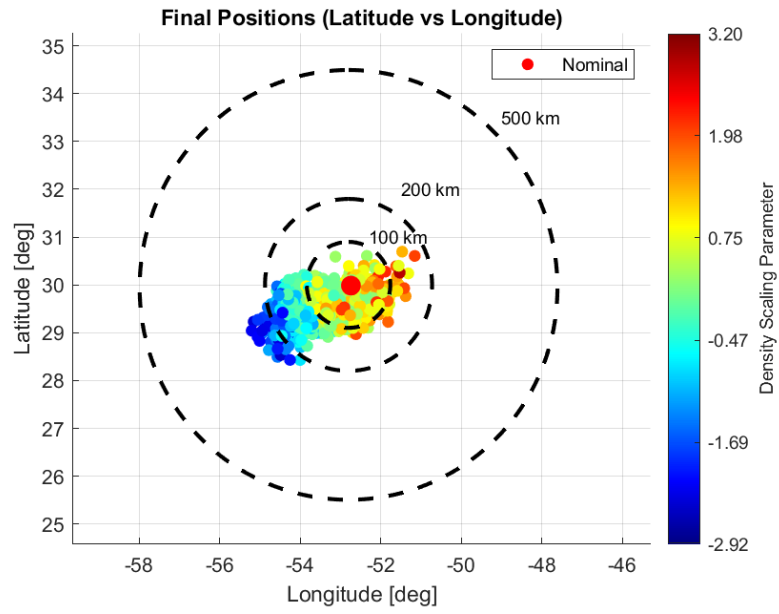


Figure 5.31: Distribution of final positions with density mapping (refined version)

In Figure 5.32, the range error distribution is presented. As previously mentioned, it is evident that the majority of cases achieve an acceptable level of accuracy, considering the subsequent final entry phase. Specifically, 99.2% of cases reach the target within 300 km, with 98.9% staying within 250 km. Furthermore, 95.7% of cases attain an accuracy of less than 200 km. These results indicate that the algorithm can be considered sufficiently robust.

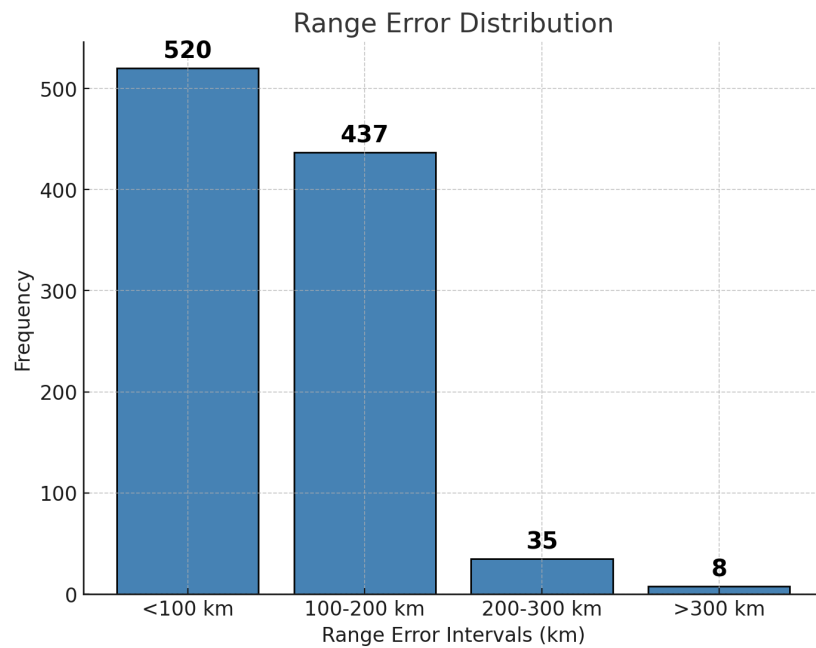


Figure 5.32: Range error distribution

In Figure 5.33 and Figure 5.34, the box plots of the range error are presented, showing the complete data and the outlier-removed version, respectively, to further analyse the results.

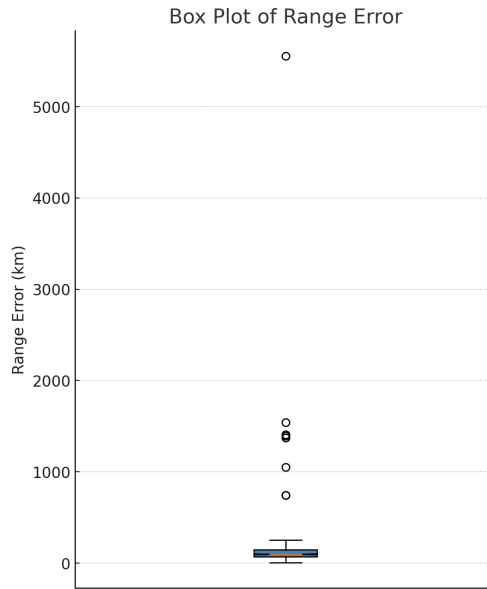


Figure 5.33: Box-plot of range error (including outliers)

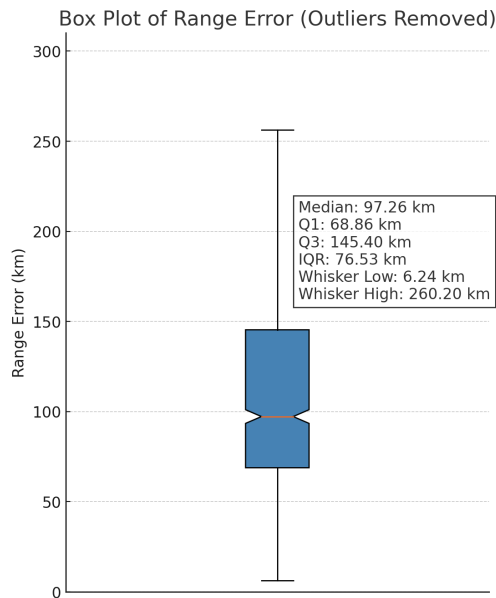


Figure 5.34: Box-plot of range error (outliers removed)

The Table 5.6 presents the results of the statistical analysis conducted on the range error and the peak values of G-load and heat flux. The maximum values reached by G-load and heat flux are within acceptable limits, while the mean and median values of the range error indicate a strong robustness of the algorithm.

Metric	Range Error (<i>km</i>)	G-Load (<i>g</i>)	Heat Flux (<i>MW/m²</i>)
Mean	119.26	3.54	4.053
Median	97.26	3.59	4.037
Maximum	5554.10	4.13	4.656
Minimum	6.24	2.14	3.488
Standard Deviation	201.96	0.27	0.2119

Table 5.6: Monte Carlo statistical summary

5.3 Future Developements

The continuous evolution of guidance algorithms and simulation models presents opportunities for further enhancements in precision and robustness. Future research can explore various avenues to refine the Numerical Predictor-Corrector (NPC) approach and extend its applicability to broader aerospace contexts.

Future developments may focus on improving the guidance algorithm by optimizing the performance of the NPC, refining its numerical stability, and enhancing its computational efficiency to ensure reliable performance across various mission scenarios.

Enhancing the accuracy of the simulation by removing simplifications in the current model, such as assuming a spherical Earth, and incorporating more sophisticated atmospheric and gravity models will be beneficial. These improvements will provide a more realistic representation of spaceflight dynamics and increase the fidelity of mission planning.

Improving the robustness of the algorithm by integrating the optimizer directly into the simulator while maintaining acceptable computational times is another important direction. Such an integration would ensure that the target is reached accurately despite uncertainties in the system, leading to a more reliable and

adaptable guidance framework.

Exploring deep learning techniques to enhance the performance of the NPC is another promising avenue. Leveraging machine learning to refine predictor-corrector processes and utilizing deep learning to predict atmospheric conditions could significantly increase the precision of the guidance system.

Extending the application of NPC-based methodologies to a wider range of spaceflight operations is a key objective. Potential applications include aerocapture, planetary landing, and aero-gravity assist maneuvers. Expanding the adaptability of NPC-based guidance strategies across different planetary environments would enhance mission efficiency and versatility.

By addressing these challenges and opportunities, future developments in NPC-based guidance algorithms will contribute to more precise, robust, and efficient spaceflight operations, ultimately supporting the next generation of aerospace exploration and mission planning.

Chapter 6

Conclusion

The objective of this thesis is to develop a skip-entry guidance strategy to effectively control a low Lift-to-Drag ratio (L/D) vehicle during re-entry from the Moon, specifically to guide it from the first Entry Interface Point (EIP) to a designated target.

The work carried out in this thesis includes the development of a high-fidelity simulation model that enables accurate trajectory simulations. A guidance algorithm is designed to control the skip-entry phase, drawing inspiration from the Apollo Guidance Algorithm although modified to incorporate a Numerical Predictor-Corrector (NPC). This is the technique used for the re-entry of Orion in the Artemis programme. This approach allows for precise bank-angle control, ensuring the vehicle reaches the target while managing thermal and structural loads. The corrector is implemented as a PID controller that adjusts the bank-angle to minimize the range error. The PID coefficients are selected using a Genetic Algorithm to minimize the final position error with respect to the target, treating the problem in terms of black-box optimization. The longitudinal and lateral dynamics are decoupled, assuming minimal cross-track errors, with lateral guidance achieved through periodic bank reversals. The nominal scenario is optimized to ensure precise targeting. A Monte Carlo analysis is performed to account for the uncertainties associated with the first EIP conditions, vehicle mass, aerodynamic parameters and atmospheric conditions. The results highlight the overall robustness of the algorithm. Low atmospheric density, combined with the low L/D of the vehicle, results in a reduced control authority.

The developed model exhibits high adaptability, allowing its application to various atmospheric maneuvers, while maintaining a balance between computational efficiency and numerical accuracy.

This thesis establishes a foundation for future research in skip-entry guidance, emphasizing the importance of advanced numerical techniques, particularly the NPC-method, in achieving precise targeting. The proposed approach is notable for its adaptability, robustness, and accuracy. There are still aspects to refine, particularly in optimizing the computational cost of high-fidelity modeling and enhancing real-time applicability. Future research could focus on improving computational efficiency and extending the method application to broader aerospace contexts. Furthermore, integrating deep learning into the predictor-corrector could enhance adaptability and performance, allowing for more efficient bank-angle selection through data-driven optimization.

Appendix A

Black Box Optimization

Black-Box Optimization (BBO) refers to the design and implementation of algorithms for problems where the structure of the objective function and constraints is unknown or not directly exploitable. This type of optimization is particularly useful when evaluating the objective function requires complex numerical simulations. In such cases, the simulator takes an input vector and returns output values $\overline{\mathbb{R}}$ instead of \mathbb{R} , as some outputs may be invalid. Assigning an infinite value to an invalid output (e.g., $f(x) = +\infty$ for an unacceptable point in minimization) allows for efficient handling of infeasible solutions, ensuring robustness in optimization processes where simulations may fail or produce inconsistent results.

BBO methods can be broadly categorized into two main approaches: direct-search and derivative-free optimization (DFO) techniques, and sequential model-based optimization (SMBO). Direct-search methods explore the solution space without relying on gradient information, which prevents them from being trapped in local minima. This makes BBO synonymous with DFO, as it circumvents the need for explicit derivative calculations. Examples of these techniques include Mesh Adaptive Direct Search (MADS), Genetic Algorithms (GA), Particle Swarm Optimization (PSO), and Simulated Annealing (SA). These methods iteratively refine candidate solutions based on performance evaluations, making them well-suited for highly complex and non-differentiable problems.

Alternatively, SMBO techniques employ surrogate models to approximate the objective function and guide the selection of promising candidate solutions. This

process involves building a predictive model based on previously observed evaluations, optimizing the surrogate model to suggest new points, and then updating the model with actual evaluations of the objective function. This iterative framework efficiently balances exploration and exploitation, enabling the discovery of near-optimal solutions in expensive or computationally demanding optimization problems.

With the growing integration of Machine Learning techniques, BBO is becoming increasingly applicable across diverse domains such as artificial intelligence, materials science, and aerospace engineering. The use of advanced learning-based methods can further refine the efficiency of BBO, particularly in cases where traditional optimization techniques struggle with high-dimensional or noisy search spaces.

Appendix B

Genetic Algorithm

During the 1950s and 1960s, independent studies were conducted to leverage evolution as an optimization tool for engineering problems. The common idea behind these systems was to evolve a population of candidate solutions using operators inspired by natural genetic variation and selection. John Holland is widely regarded as the founding father of genetic algorithms, having introduced the concept in the 1970s [17].

A genetic algorithm is a method that allows the transition from one population of "chromosomes" (candidate solutions) to another through "natural selection" combined with genetic-inspired operators such as crossover, mutation, and inversion. The selection operator determines which chromosomes in the population will reproduce, with fitter chromosomes on average generating more offspring.

A GA operates through populations of chromosomes, where selection favors the most promising solutions, crossover combines genetic material to create new offspring, and mutation introduces variations to maintain genetic diversity and prevent premature convergence. These mechanisms interact to ensure a balance between exploring new potential solutions and exploiting high-performing ones.

A GA typically requires a fitness function that assigns a score to each chromosome in the current population, reflecting how well it solves the given problem. The basic steps of a genetic algorithm are:

1. **Initialization:** Random creation of an initial population.
2. **Evaluation:** Calculation of the fitness $f(x)$ of each chromosome x in the

population.

3. Generation of a new population:

- **Selection:** Choice of parent chromosome pairs based on their fitness. Selection is performed with replacement, meaning the same chromosome can be chosen multiple times.
- **Crossover:** With probability p_c , two parents are crossed at a random point to form two offspring. If no crossover occurs, the offspring are exact copies of their parents.
- **Mutation:** Each bit of the new chromosomes can be flipped with probability p_m .
- **Replacement:** The new population replaces the previous one.

4. Iteration: Steps 2–3 are repeated until a stopping criterion is met (maximum number of generations or population convergence).

Each iteration is called a generation, and the full sequence of generations forms a run. At the end of a run, the population typically contains one or more highly adapted chromosomes.

Compared to traditional optimization methods like Newton’s method or gradient descent, genetic algorithms exhibit key differences:

- **Population-based search:** Traditional methods optimize from a single starting point, whereas GAs work on an entire population, enhancing robustness and reducing the risk of being trapped in local optima.
- **Derivative-free optimization:** GAs do not require information about function derivatives, making them suitable for non-differentiable or complex objective functions.
- **Probabilistic transition operators:** While classical methods use deterministic operators, GAs rely on probabilistic operators to generate new solutions, ensuring broader exploration of the solution space.

Genetic algorithms are a powerful and flexible optimization tool applicable to a broad range of problems. Their effectiveness depends on choosing appropriate parameters, such as population size, crossover and mutation probabilities, and stopping criteria. Advanced GA variants, such as Genetic Programming or Hybrid Genetic Algorithms, can further enhance performance for specific applications.

Bibliography

- [1] NASA. *The Apollo Program*. URL: <https://www.nasa.gov/the-apollo-program/> (cit. on p. 1).
- [2] NASA. *Artemis*. URL: <https://www.nasa.gov/the-apollo-program/> (cit. on p. 1).
- [3] B. Murray. *Orion during reentry*. URL: <https://www.planetary.org/space-images/orion-reentry> (cit. on p. 2).
- [4] N. H. Kemp and F. R. Riddell. «Heat Transfer to Satellite Vehicles Re-entering the Atmosphere». In: *Journal of Jet Propulsion* 27.2 (1957), pp. 132–137 (cit. on p. 8).
- [5] M. E. Tauber and K. Sutton. «Stagnation-point radiative heating relations for earth and Mars entries». In: *Journal of Spacecraft and Rockets* 28 (1991), pp. 40–42 (cit. on p. 9).
- [6] NASA. *Orion*. URL: <https://images.nasa.gov/details/ED08-0230-362> (cit. on p. 10).
- [7] SpaceX. *SpaceX unveils sleek, reusable Dragon crew capsule*. URL: <https://www.newscientist.com/article/dn25652-spacex-unveils-sleek-reusable-dragon-crew-capsule/> (cit. on p. 10).
- [8] D. J. Lickly, H. R. Morth, and B. S. Crawford. *Apollo reentry guidance*. Tech. rep. Space Guidance Analysis Group, Massachusetts Institute of Technology, Instrumentation Laboratory, 1963 (cit. on p. 12).
- [9] S. Hendrickson Bairstow. «Reentry Guidance with Extended Range Capability for Low L/D Spacecraft». Engineering and Applied Science (Aeronautics). B.S. Thesis. California Institute of Technology, 2004 (cit. on pp. 16, 17).

- [10] J. L.G. Guirao H. Chen K. Zhao and D. Cao. «Analytical predictor-corrector entry guidance for hypersonic gliding vehicles». In: *International Journal of Nonlinear Sciences and Numerical Simulation* 21.5-6 (Dec. 2020), pp. 567–579 (cit. on p. 16).
- [11] J. R. Rea and Z. R. Putnam. *A Comparison of Two Skip Entry Guidance Algorithms*. Tech. rep. Houston, Texas, 77058, USA: NASA Johnson Space Center and The Charles Stark Draper Laboratory, Inc., 2025 (cit. on pp. 16, 17).
- [12] J. L. DiCarlo. «Aerocapture Guidance Methods for High Energy Trajectories». B.S. Aeronautical and Astronautical Engineering. United States Air Force Academy, 2001 (cit. on p. 17).
- [13] C. Brunner and P. Lu. «Comparison of Fully Numerical Predictor-Corrector and Apollo Skip Entry Guidance Algorithms». In: *American Astronautical Society* (July 2014). Published online: 17 July 2014 (cit. on p. 19).
- [14] C. Brunner and P. Lu. «Skip Entry Trajectory Planning and Guidance». In: *Journal of Guidance Control Dynamics* 31 (Sept. 2008), pp. 1210–1219 (cit. on p. 22).
- [15] United States Committee on Extension to the Standard Atmosphere. *U.S. Standard Atmosphere, 1962*. Washington, D.C.: United States Government Printing Office, 1962 (cit. on p. 25).
- [16] A. E. Bryson. *Applied Optimal Control: Optimization, Estimation and Control*. 1st. Routledge, 1975 (cit. on p. 33).
- [17] J. H. Holland. *Adaptation in Natural and Artificial Systems: An Introductory Analysis with Applications to Biology, Control, and Artificial Intelligence*. The MIT Press, Apr. 1992. ISBN: 9780262275552 (cit. on p. 70).
- [18] S. Alarie, C. Audet, A. Gheribi, M. Kokkolaras, and S. Le Digabel. «Two decades of blackbox optimization applications». In: *EURO Journal on Computational Optimization* 9 (Sept. 2021), p. 100011.
- [19] U. Bodenhofer. *Genetic Algorithms: Theory and Applications*. Jan. 1999.
- [20] M. Mitchell. *An Introduction to Genetic Algorithms*. The MIT Press, Feb. 1996. ISBN: 9780262280013.

- [21] Wataru Kumagai and Keiichiro Yasuda. «Black-Box Optimization and Its Applications». In: *Innovative Systems Approach for Facilitating Smarter World*. Ed. by Toshiya Kaihara, Hajime Kita, Shingo Takahashi, and Motohisa Funabashi. Singapore: Springer Nature Singapore, 2023, pp. 81–100. ISBN: 978-981-19-7776-3.

Acknowledgements

Ringrazio il mio relatore Lorenzo Casalino e il team di Mission Analysis e Operations di Thales Alenia Space per avermi sostenuta e seguita nella stesura di questa tesi.